



HAL
open science

10Be chronology of deglaciation and ice-dammed lake regression in the vicinity of the Mylodon Cave (Cerro Benítez, Patagonia, Chile)

Igor Girault, Dominique Todisco, Attila Çiner, Mehmet Akif Sarıkaya, Cengiz Yıldırım, Amélie Quiquerez, Fabiana Martin, Luis Borrero, Derek Fabel, Philippe Grandjean, et al.

► To cite this version:

Igor Girault, Dominique Todisco, Attila Çiner, Mehmet Akif Sarıkaya, Cengiz Yıldırım, et al.. 10Be chronology of deglaciation and ice-dammed lake regression in the vicinity of the Mylodon Cave (Cerro Benítez, Patagonia, Chile). *Quaternary Science Reviews*, 2022, 278, pp.107354. 10.1016/j.quascirev.2021.107354 . halshs-03560016

HAL Id: halshs-03560016

<https://shs.hal.science/halshs-03560016>

Submitted on 22 Jul 2024

HAL is a multi-disciplinary open access archive for the deposit and dissemination of scientific research documents, whether they are published or not. The documents may come from teaching and research institutions in France or abroad, or from public or private research centers.

L'archive ouverte pluridisciplinaire **HAL**, est destinée au dépôt et à la diffusion de documents scientifiques de niveau recherche, publiés ou non, émanant des établissements d'enseignement et de recherche français ou étrangers, des laboratoires publics ou privés.



Distributed under a Creative Commons Attribution - NonCommercial 4.0 International License

¹⁰Be chronology of deglaciation and ice-dammed lake regression in the vicinity of the Mylodon Cave (Cerro Benítez, Patagonia, Chile)

Igor Girault¹, Dominique Todisco¹, Attila Çiner², Mehmet Akif Sarıkaya², Cengiz Yıldırım², Amélie Quiquerez³, Fabiana Martin⁵, Luis Borrero⁶, Derek Fabel³, Philippe Grandjean⁷, Carole Nehme¹, Damase Mouralis¹

1: Département de Géographie, Université de Rouen, CNRS: UMR 6266 (France)

2: Eurasia Institute of Earth Sciences, İstanbul Technical University (Turkey)

3: Scottish Universities Environmental Research Centre, East Kilbride, Glasgow (United Kingdom)

4: Archéologie, Terre, Histoire, Sociétés (ArTeHis), Université de Bourgogne, CNRS: UMR 6298 (France)

5: Centro de Estudios del Hombre Austral, Instituto de la Patagonia, Universidad Magallanes (Chile)

6: Instituto Multidisciplinario de Historia y Ciencias Humanas, CONICET, Universidad de Buenos Aires (Argentina)

7: Laboratoire de Géologie de Lyon, Université de Lyon 1, CNRS: UMR 5276 (France)

Abstract

Located 51.5°S in the vicinity of the Southern Patagonian Ice Field, Cerro Benítez and the glacial valley of Lago Sofía host several caves and rock shelters that were occupied by megafauna and humans during the Late Pleistocene, including the Mylodon Cave and two of the oldest archaeological sites in Patagonia. During the last glaciation, Cerro Benítez was alternately covered by the Patagonian Ice Sheet and surrounded by an ice-dammed lake which restricted the access to the caves and rock shelters located under its uppermost level, 155 m a.s.l. This study aims to provide a detailed chronology of the deglaciation and lake regression in Cerro Benítez. The glacial fluctuations and the variations of lake level were reconstructed from multi-scale, remote-sensing data and field geomorphological mapping. In addition, we calculated the surface exposure age of 11 erratic blocks located above and on the lacustrine erosional platform using terrestrial cosmogenic ¹⁰Be in order to date ice downwasting and lake regression, respectively. Dates of ice downwasting and lake regression events were modelled from prior surface exposure ages using Bayesian statistics. The results suggest that the Patagonian Ice Sheet locally thinned by at least 300 m during MIS 3 in the aftermath of a major glacial advance. Following deglaciation, the ice-dammed lake experienced a slow local regression (*ca.* 2.5 mm.a⁻¹) until 16.9 ka B2k, interpreted as the result of lake basin tilting due to differential post-glacial isostatic rebound. This initial phase of lake regression was followed by a faster regression caused by the reversal of the lake drainage between 16.9 and 15.4 ka B2k. We assess the chronological model by comparison with uplift and lakeshore erosion rates from the literature and eventually discuss the implications for megafaunal colonisation of the area.

Keywords: Pleistocene; Glaciation; South America; Cosmogenic isotopes; Geomorphology, glacial; Chronological modelling; Mylodon Cave.

1. Introduction

The Patagonian Andes currently host the three largest ice fields of the Southern Hemisphere excluding Antarctica: the Northern Patagonian Ice Field (46.5 to 47.5°S), the Southern Patagonian Ice Field (48.5 to 51.0°S) and the Cordillera Darwin Ice Field (54.5 to 55.0°S), spanning a total of more than 19,000 km² (Davies and Glasser, 2012). Since the nineteenth century, the description and mapping of glacial landforms and deposits have indicated that Patagonian glaciers were more extended in the past and repeatedly formed a continuous, elongate ice sheet between 37.0 and 56.0°S during the Quaternary period: the Patagonian Ice Sheet (Nordenskjöld, 1899; Caldenius, 1932; Figure 1). During the Last Glaciation, the Patagonian Ice Sheet reached a maximal extent of near 500,000 km² (Davies *et al.*, 2020) and supplied 52 eastward-flowing, outlet ice lobes (Glasser *et al.*, 2008). Following the global Last Glacial Maximum (LGM), *ca.* 19.0-26.5 ka BP (Clark *et al.*, 2009), the Patagonian Ice Sheet underwent significant deglaciation and its extent eventually decreased by 66.1 % between 20.0 and 15.0 ka (Davies *et al.*, 2020).

Located 51.5°S, in the Chilean province of Última Esperanza, Cerro Benítez (554 m a.s.l.) is a summit of the Patagonian fold and thrust belt bordered by the glacial valley of Lago Sofía, to the north, and the Última Esperanza fjord, to the south (Figure 1). Cerro Benítez and the Lago Sofía valley host several caves and rock shelters located on a former proglacial lakeshore (Ferruglio, 1950; Stern *et al.*, 2011). Among them, the Mylodon Cave aroused a considerable palaeontological interest following the incidental excavation of extinct ground sloth *Mylodon* material in 1895 (Hauthal, 1899; Emperaire and Laming, 1954; Martinic, 1996; Borrero and Martin, 2012). Since then, Late Pleistocene megafaunal assemblages were found in thirteen caves and rock shelters in Cerro Benítez and the Lago Sofía valley (Table 1; Figure 2). In addition with Late Pleistocene megafaunal material, two caves (Cueva Lago Sofía 1 and Cueva del Medio) yielded some of the earliest evidences of human presence in Patagonia, dated from 13.6-13.3 ka cal. BP (Nami, 1985-1986; Prieto, 1991; Nami and Nakamura, 1995; Martin *et al.*, 2015). The rich palaeontological and archaeological heritage of Cerro Benítez led to the creation of the Mylodon Cave Natural Monument, a protected area administered by the Corporación Nacional Forestal (CONAF) since 1993.

Previous works indicated that an eastward-flowing ice lobe and an ice-dammed lake alternately occupied the Última Esperanza fjord and the Lago Sofía valley during the Last Glaciation (Moreno, 1899; Caldenius, 1932; Ferruglio, 1950; Sagredo *et al.*, 2011; Stern *et al.*, 2011; García *et al.*, 2018). Hence, Cerro Benítez remained inaccessible to megafauna and humans until the ice margin retreated and caves and rock shelters emerged from the lake. The existing chronology of the deglaciation and lake regression relies on ¹⁴C ages only, which provides minimal dates of ice margin retreat and lake regression only. The actual chronology of the deglaciation and the subsequent regression of the ice-dammed lake therefore remains a matter of speculation, in the absence of an extensive geomorphological study of Cerro Benítez (Stern *et al.*, 2011; Martin and Borrero, 2017; Todisco *et al.*, 2018). This study aims to establish a detailed chronology of the deglaciation of Cerro Benítez and the ice-dammed lake regression based on multi-scale geomorphological mapping and chronological modelling constrained by surface exposure dating using terrestrial cosmogenic nuclides, in order to identify the processes of lake regression and better constrain the palaeogeography of Cerro Benítez at the time of megafaunal colonisation.

2. Geomorphological setting

2.1. Lithology and structure of the bedrock

Cerro Benítez is located on the outcrop belt of the Lago Sofía Conglomerate, a 390 to 440 m thick series of bathyal turbidites and gravity flow deposits belonging to the Late Cretaceous, Cerro Toro Formation. The Lago Sofía Conglomerate was deposited along the axial foredeep of the Magallanes foreland basin. The conglomerate is made up

of well-rounded, magmatic gravels and blocks up to 42 cm long and occurs as units up to 80 m thick, interbedded with sandstone and mudstone units 10 to 100 m thick (Hubbard *et al.*, 2008; Romans *et al.*, 2011).

During the Oligocene-Miocene, the Cerro Toro Formation folded along a north-south anticline axis in response to the eastward Castillo thrust (Fosdick *et al.*, 2011). The anticline hinge passes near the top of Cerro Benítez, dips southward between Cueva del Medio and Cueva Chica and terminates in Cerro Torta, 1 km south of Cerro Benítez (Figure 2).

The Cerro Toro Formation is overlain by the Late Cretaceous Tres Pasos Formation, composed of interbedded sandstone and mudstone units. The Tres Pasos Formation outcrops 500 m east of Cerro Benítez as a north-south homoclinal scarp culminating 230 m a.s.l. (Figure 2), resulting from eastward tilting during the Miocene in response to the Toro thrust (Fosdick *et al.*, 2011; Romans *et al.*, 2011).

2.2. Moraine complexes

The Última Esperanza ice lobe was an eastward-flowing, outlet glacier formed by the coalescence of several tributary glaciers at the eastern margin of the Patagonian Ice Sheet, during the last glaciation (Sagredo *et al.*, 2011). Successive advances of the Última Esperanza ice lobe deposited two concentric, horseshoe-shaped moraine complexes, composed of multiple recessional moraine ridges, and separated by an outwash plain (Figure 1). The outer moraine complex, named “Río Turbio moraine complex” by Sagredo *et al.* (2011), forms a 100 km long latero-frontal arc dissected by the Río Turbio valley. The inner moraine complex forms an 80 km long latero-frontal arc dividing the Atlantic and Pacific drainage basins, previously identified as “Balmaceda moraines” by Caldenius (1932) and named “Arauco moraine complex” by Sagredo *et al.* (2011). The Arauco moraine complex extends northward as the Dos Lagunas moraine, buttressed on the western side of Sierra Dorotea and culminating 300 m a.s.l., 5 km east of Cerro Benítez (Sagredo *et al.*, 2011; García *et al.*, 2014).

Caldenius (1932) initially ascribed the Río Turbio and Arauco moraine complexes to the penultimate glaciation, or “Gotiglacial”. However, recent work using absolute dating methods evidenced that both moraine complexes were formed during the Last Glaciation. Sagredo *et al.* (2011) obtained for the first time three ^{10}Be surface exposure ages of erratic blocks from the Dos Lagunas moraine which ranged from 34.7 ± 1.9 to 37.8 ± 4.2 ka. More recently, García *et al.* (2018) dated the Río Turbio advance *ca.* 45.7 ka and the Arauco advance *ca.* 32.4 ka, based on the median ^{10}Be surface exposure age of 8 and 12 erratic blocks, respectively (Table 2; Figure 1).

Following the Arauco advance, the tributary glaciers of the Última Esperanza separated and experienced several more restricted readvances. The northward-flowing tributary occupying the Obstrucción fjord deposited a 40 km long, latero-frontal moraine arc around Lago Aníbal Pinto, flattened at the top by lacustrine erosion between 125 and 170 m a.s.l., named “Aníbal Pinto moraine complex” by Sagredo *et al.* (2011). In addition, an eastward-flowing tributary readvanced to the present-day location of Puerto Natales and deposited the Antonio Varas moraine, composed of discontinuous ridge segments, culminating 60 m a.s.l., forming a latero-frontal arc extending on both sides of the fjord (Figure 1). In the absence of absolute dating, the age of the moraines remains speculative (Sagredo *et al.*, 2011).

2.3. Erosional platforms

Four sedimentary sections previously described by Sagredo *et al.* (2011), exhibiting glaciolacustrine and subaqueous fan deposits truncated and overlain by till (Dorotea Crossroad, Dorotea Pits, Dumestre, and Puerto Natales; Figure 1) indicate that the Arauco advance and the subsequent retreat of the ice margin occurred in a glaciolacustrine environment. As the Última Esperanza ice lobe retreated, an ice-dammed lake named “Lago Consuelo” filled the depression delimited by the Arauco moraine complex, to the east, and the Dos Lagunas moraine, to the north (Moreno, 1899; Caldenius, 1932; Sagredo *et al.*, 2011; Stern *et al.*, 2011). The lake level variations can be reconstructed from an extensive assemblage of glaciolacustrine landforms and deposits, or “glaciolacustrine landsystem” (Teller, 2003; Davies *et al.*,

2020), comprising raised deltas, beaches, palaeoshorelines and two main erosional platforms mostly referred to as “terraces” in the existing literature (**Figure 1; Table 3**).

The upper erosional platform is carved in bedrock as well as glacial and glaciofluvial deposits between 120 and 170 m a.s.l., truncating the inner side of the Arauco moraine complex and the frontal arc of the Aníbal Pinto moraine complex and surrounding Cerro Benítez and the Lago Sofía valley (**Caldenius, 1932; Feruglio, 1950; Sagredo et al., 2011; Stern et al., 2011; Figure 1**). The uppermost lake level is marked by a 135 m a.s.l. channel incised through the Arauco moraine complex, that drained the lake to the Atlantic Ocean. The uppermost palaeoshoreline rises westward from 125 to 170 m a.s.l. as a result of differential post-glacial isostatic rebound, in agreement with the predicted ice thickness gradient (**Stern et al., 2011; Figure 1**). Lago Consuelo expanded northward as deglaciation of the Prat valley opened a connection with Lago Tehuelche, reaching a maximal extent of near 1 400 km² (**Davies et al., 2020**). In the Lago Tehuelche area, the subsequent drainage of Lago Tehuelche to Lago Consuelo resulted in a fall of the lake level from its uppermost erosional platform, 240-260 m a.s.l. and to the development of a 150-165 m a.s.l. erosional platform (**Solari et al., 2012; García et al., 2014**).

Deglaciation of the Obstrucción fjord triggered the reversal of the lake drainage to the Magallanes lake, occupying the Otway and Skyring fjord, and a considerable fall of the lake level, as indicated by a lower erosional platform carved on the shore of the Última Esperanza fjord and around Lago Balmaceda between 20 and 30 m a.s.l. (**Feruglio, 1950; Stern et al., 2011; Kilian et al., 2013; Figure 1**). After the Magellan lake eventually drained to the Pacific Ocean, a marine erosional platform developed between 5 and 8 m a.s.l. along the eastern shore of the Última Esperanza fjord (**Caldenius, 1932; Sagredo et al., 2011; Figure 1**).

2.4. Existing chronology of ice margin retreat and lake regression

The existing chronology of deglaciation and lake regression posterior to the Arauco advance is constrained by ¹⁴C ages from the sedimentary and palaeontological records.

A set of ¹⁴C ages of organic deposits from eight sedimentary cores and sections obtained by **Sagredo et al. (2011)** indicates a minimal date of ice margin retreat of 17.3 ka cal. BP in Vega Benítez, 215 m a.s.l., and a minimal date of lake regression of 15.2-15.6 ka cal. BP in Pantano Dumestre, 77 m a.s.l. (**Table 1; Figure 1**). The ¹⁴C ages of the palaeontological material from the caves and rock shelters of Cerro Benítez and the Lago Sofía valley represent additional minimal ages of ice margin retreat and lake regression (**Todisco et al., 2018**). The earliest dated palaeontological material predates the minimal date of lake regression estimated in Pantano Dumestre in 8 caves (**Table 1**). In Cueva Chica, an astragalus of *Lama gracilis* dated 17.9-18.3 ka cal. BP also predates the minimal date of ice margin retreat estimated in Vega Benítez (**Martin et al., 2013; Table 1**).

3. Material and methods

3.1. Geomorphological mapping

We completed two geomorphological maps: an updated geomorphological map of the Última Esperanza fjord, and the first geomorphological map of Cerro Benítez. The map of the Última Esperanza fjord is a critical synthesis of previous geomorphological mapping of the area based on both remote-sensing and field data (**Caldenius, 1932; Sagredo et al., 2011; García et al., 2014; García et al., 2018**) and remote-sensing data only (**Glasser and Jansson, 2008; Darvill et al., 2014**). The maps were georeferenced and compiled in a Geographic Information System (GIS), then revised after the interpretation of remote-sensing data comprising satellite images (Google Earth imagery) and a digital elevation model with a resolution of 3 arc seconds (SRTM 90m DEM v4.1). Landforms and deposits were mapped on a vector graphic

editor for greater ergonomics. The entire area was mapped at the scale of 1:500,000 (**Figure 1**). In addition, six smaller areas of specific interest were mapped at the scale of 1:50,000 (**Figure 3**).

The map of Cerro Benítez is based on both remote-sensing and field data. We followed the seven-step workflow specifically designed by [Chandler *et al.* \(2018\)](#) for field mapping of glacial landforms and deposits:

1-3. Data procurement, pre-processing and reconnaissance mapping. We used the MicMac photogrammetry software (<https://micmac.ensg.eu/index.php/Accueil>) to build a Digital Surface Model (DSM) of the area with a horizontal resolution of 50 cm from a set of tristereographic, panchromatic Pléiades satellite images. Prominent landforms were mapped in a GIS in order to select the areas of priority interest for subsequent field mapping.

4. Field mapping. Cerro Benítez was covered with an extensive field survey after four campaigns between 2017 and 2020. Superficial deposits were characterised based on the field facies analysis of 6 existing natural outcrops and 2 additional test pits (**Table 4**). Orientation and dip of erosional landforms and beddings were measured with a compass clinometer. The orientation was systematically corrected by subtracting the magnetic declination. In support of the ground operations, we used aerial drone photography to investigate the southern side of Cerro Benítez. We used a DJI Mavic Pro for reconnaissance survey and oblique aerial photography and a DJI Phantom IV for nadir aerial photography. Landforms and deposits were mapped on hard-copy, orthorectified satellite images.

5-7. Data processing, digital mapping and map production. Hard-copy maps were reproduced on a vector graphic editor. The entire area was mapped at the scale of 1:50,000 (**Figure 2**). In addition, the area of the Mylodon Labyrinth was mapped at the scale of 1:5,000 (**Figure 4**).

3.2. Terrestrial cosmogenic ^{10}Be surface exposure dating

Terrestrial (or *in situ*) cosmogenic nuclides are produced by nuclear reactions involving nuclides present at the Earth's surface and incident secondary cosmic rays. Terrestrial cosmogenic ^{10}Be originates in quartz from spallation and muon capture by O and Si ([Gosse and Philips, 2001](#)). Considering an attenuation length of *ca.* 160 g.cm⁻² ([Gosse and Philips, 2001](#); [Balco *et al.*, 2008](#)), the production of terrestrial cosmogenic ^{10}Be decreases by a factor e^{-1} under 1.7 m of ice, or 1.6 m of water. ^{10}Be has a half-life of 1.39 Ma ([Korschinek *et al.*, 2010](#)). For these reasons, terrestrial cosmogenic ^{10}Be have been widely used to date the surface exposure of glacial landforms and deposits over the Quaternary period ([Davies, 2021](#)). Terrestrial cosmogenic ^{10}Be surface exposure ages of erratic blocks have been mostly used to date former ice margin positions, notably in Patagonia since the works of [Kaplan *et al.* \(2004\)](#), but also, in fewer circumstances, to date proglacial lake regression ([Fabel *et al.*, 2010](#); [Davies *et al.*, 2018](#); [Thorndycraft *et al.*, 2019](#)).

In order to estimate the rate of ice downwasting in Cerro Benítez, we sampled four erratic blocks located above the lacustrine erosional platform, approximately every 100 m from near the top of Cerro Benítez (512 m a.s.l.), as a dipstick, following the strategy of [Boex *et al.*, 2013](#). In addition, seven erratic blocks were sampled on the erosional lacustrine platform between 148 and 136 m a.s.l. Erratic blocks located on the lacustrine erosional platform may be either inherited from older glacial deposits, or deposited by icebergs. In both cases, the production of terrestrial cosmogenic ^{10}Be started as the water depth decreased, leaving the bottom of the lake exposed to the cosmic rays (**Figure 5**). Hence, we assume that the surface exposure age date the emergence of the erratic blocks.

We selected erratic blocks located either on local summits, or on flat areas with little chance of being reworked by mass wasting. Weathered and denuded blocks were avoided. At least 1 kg of rock was sampled with a hammer and a chisel at the top of each block up to 3 cm below the surface. Coordinates and elevation of each sample were recorded with a hand-held GPS and topographic shielding angles were measured with a clinometer. Photographs of the sampled blocks are presented in **Figure 6**.

Rock samples were crushed and sieved at Kozmo-Lab, İstanbul Technical University (<https://www.kozmo-lab.itu.edu.tr/en>). The 0.25-0.71 mm grain size fraction was rinsed with milli-Q water and leached overnight with a 10 % HNO₃ solution. Non-magnetic minerals were collected with a Frantz magnetic separator and sent to the Scottish Universities Environmental Research Centre, University of Glasgow, for further preparation. Quartz was extracted by froth floatation and purified by leaching in a boiling H₃PO₄ solution and with a 2 % HF and HNO₃ solution in ultrasonic bath. Quartz purity was assessed by measuring the amount of native Al in the sample with a flame atomic absorption spectrometer. All samples yielded Al concentrations less than 130 mg.g⁻¹. Between 1 and 18 g of pure quartz per sample were dissolved in an HF and HNO₃ solution in addition with a 215 to 225 µg low background carrier of ⁹Be. BeO was extracted after quartz totally dissolved. Be isotope concentrations were measured with a 5 MV Tandem Accelerator Mass Spectrometer (AMS) at the SUERC AMS Laboratory. Measured ¹⁰Be/⁹Be ratios were normalised to the 07KNSTD standard and corrected with a mean procedural blank ¹⁰Be/⁹Be ratio of 3.75 × 10⁻¹⁵.

Surface exposure ages were calculated with the online exposure age calculator CRONUS v3 (<https://hess.ess.washington.edu>; Balco *et al.*, 2008). Sample density was assumed as 2.65 g.cm⁻³. Erosion was neglected because unequivocally weathered surfaces were avoided, following García *et al.* (2018).

We used the Lifton-Sato scaling scheme (Lifton *et al.*, 2014) and the production rate model of Borchers *et al.* (2016), for purpose of comparison with the recent compilation of surface exposure ages in Patagonia by Davies *et al.* (2020). Ages calculated with alternate production rates and scaling schemes are less than 10 % different (Table 2).

3.3. Chronological modelling

Bayesian statistics are increasingly used in chronological modelling applied to the study of landform development (e.g. Chiverell *et al.*, 2009; Bendle *et al.*, 2017b; Thorndycraft *et al.*, 2019; Genuite *et al.*, 2021). Chronological modelling using Bayesian statistics aims to obtain absolute chronological models (or “posterior dates”) from a set of prior, absolute dates arranged in a hypothetical, relative chronology.

In order to build a chronological model of deglaciation and lake regression from our set of surface exposure ages, we used the chronological modelling software Chronomodel v2.0.18 (<https://github.com/Chronomodel/chronomodel>; Lanos and Philippe, 2015; Lanos and Dufresne, 2019). The posterior distributions of the dates were calculated with a Metropolis-Hastings algorithm using an adaptative Gaussian random walk for the terrestrial cosmogenic ¹⁰Be surface exposure dates, and the posterior distribution of the calibrated date for the ¹⁴C date. We used three Markov chains with a burn-in phase of 1,000 iterations, an adaptation phase of 500 iterations per batch with a maximum of 20 batches, and an acquisition phase of 100,000 iterations. Prior and posterior distributions of the dates were calibrated B2k.

4. Results

4.1. Remote-sensing data mapping

Some of the landforms previously mapped by Glasser and Jansson (2008), Darvill *et al.* (2014) and García *et al.* (2018) were critically revised based on a set of identification criteria adapted from Glasser and Jansson (2008), Darvill *et al.* (2014) and Bendle *et al.* (2017a). The surface mapped as a kame terrace by García *et al.* (2018) is rather interpreted as a lacustrine erosional platform, following the opinion of Caldenius (1932) and Sagredo *et al.* (2011), because it is backed by raised lakeshore landforms and deposits (Figure 3.A-D).

We identified a 35 km long latero-frontal moraine arc composed of several concentric moraine ridges on both sides of the Última Esperanza fjord previously mapped by Glasser and Jansson (2008) and two new ridge segments on the eastern side of the fjord (Figure 1). We name it “Ballena moraine complex”. The lateral ridges are buttressed on the

northern side of Cerro Ballena with a maximal elevation decreasing eastward from 280 to 120 m a.s.l. (**Figure 3.E**). The frontal ridge culminates 95 m at its northernmost extremity and 80 m at its southernmost extremity (**Figure 3.F**).

4.2. Field mapping

4.2.1. Glacial and glaciofluvial landforms and deposits

- **Roches moutonnées:** Roches moutonnées are asymmetrical, convex erosional landforms resulting from the heterogeneous resistance of the bedrock to the subglacial abrasion, with an abraded up-flow face and a quarried down-flow face (**Glasser and Bennett, 2004**). Roches moutonnées occur between 200 and 350 m a.s.l. and between 145 and 160 m a.s.l. The roches moutonnées located between 200 and 350 m a.s.l. are shaped on westward-dipping conglomerate units and indicate an eastward ice flow (**Figure 7.A**). The roches moutonnées located between 145 and 160 m a.s.l. occur on both northern and southern side of Cerro Benítez. On the northern side, roches moutonnées are shaped on discordant conglomerate injectites (**Hubbard et al., 2007**) and indicate a N040° ice flow (**Figure 7.B**). On the southern side, roches moutonnées are shaped on westward-dipping conglomerate units and indicate an eastward ice flow (**Figure 7.C**). Smaller-scale subglacial erosion marks are not preserved because of the superficial weathering of the conglomerate, with the exception of a possible trail of crescentic gouges (**Glasser and Bennett, 2004; Figure 7.B**).
- **Subglacial meltwater channels:** Several channels carved in the bedrock occur on the southern side of Cerro Benítez. Considering that the channels are disconnected from the present-day drainage system and some have an undulating long profile, we interpret them as the product of subglacial meltwater erosion (**Glasser and Bennett, 2004; Greenwood et al., 2007**).

The largest channel network is located east of the Mylodon Cave. We name it “Mylodon Labyrinth” (**Figure 7.D**). The channel network is composed of a 620 m long, up to 17 m wide, main anastomosed channel with an overall orientation of N105°, and several, smaller tributary channels carved along N040° fractures (**Figure 4**). The main channel is carved to a depth of 2 m below the lowest channel bank, with an inception located 140 m a.s.l. and a termination 143 m a.s.l. A smaller, 200 m long, 130 m wide anastomosed network occurs between 145 and 150 m a.s.l. at the top of a roche moutonnée, south of Cueva del Medio (**Figure 7.E**). We name it “Zorro Labyrinth”. The channels are carved to a depth of 2.5 m below the lowest channel bank, along a network of fractures oriented N130° to N140°.

Subglacial meltwater channels are formed by the drainage of subglacial meltwater sourced from the melting of the glacier sole, catchment of supraglacial streams or catastrophic drainage of supraglacial lakes (**Fountain and Walder, 1998; Glasser and Hambrey, 1998**). The subglacial meltwater flow is directed by the ice overburden pressure gradient (**Glasser and Bennett, 2004; Greenwood et al., 2007**). Considering that subglacial erosion exploits the surfaces of least resistance, the subglacial channel network accommodates the orientation of the meltwater flow to the structural constraints of the bedrock (**Sagawaki and Hirakawa, 1998**). Hence, the general orientation of the subglacial channel networks is consistent with the orientation of the roches moutonnées located at the same altitude, indicating an eastward ice flow on the southern side of Cerro Benítez.

- **Till:** Several till facies occur in Cerro Benítez as massive, unsorted, matrix-supported diamicton (Dmm) composed of sharp-edged, angular clasts embedded in a variable proportion of matrix, and massive, sandy-matrix, clast-supported diamicton (Dcm) composed of sharp-edged angular to moderately rounded clasts (**Table 4**). The Dmm(s) facies presents anastomosed, subhorizontal fractures interpreted as the result of sediment shearing and water escape under a sliding, temperate glacier sole (**van de Meer et al., 2003; Evans et al., 2006**). In the absence of macroscopic evidence of subglacial deformation, the depositional processes of the other till facies remain

uncertain, although the spatial transitions with the Dmm(s) facies suggest that the Dmm₁ and Dmm₃ facies also deposited in a subglacial environment (**Table 4**).

A continuous till belt covers the southern side of Cerro Benítez. The Portería section is a 500 m long, 1 to 2 m high section located between 92 and 120 m a.s.l., along the road west of the Mylodon Cave. The Dmm₁ facies outcrops from 92 m a.s.l. (**Figure 8.A**) and laterally passes to the Dmm(s) facies at 100 m a.s.l. Between 110 and 120 m a.s.l., the Lago Sofía conglomerate is truncated and overlain by a 50 cm thick Dmm₃ unit and a 50 cm to 1 m thick Dmm(s) unit (**Figure 8.B**). The Silla del Diablo section is a 1,700 m long, 1 to 3 m high section located between 108 and 138 m a.s.l., along the road east of the Mylodon Cave. The Lago Sofía conglomerate is truncated and overlain by a Dmm(s) unit with a maximal thickness of 2 m at the intersection with two east-west thalwegs. The Dmm(s) unit thins upward until it disappears at 128 m a.s.l., in a bevel-shaped contact with the bedrock (**Figure 8.C**). The Caranchos pit was dug 136 m a.s.l. on the southern side of Cerro Benítez (**Figure 8.D**). The Cerro Toro Formation mudstone is truncated at a depth of 70 cm and overlain by a 40 cm thick, Dmm₁ unit covered by an organic-rich topsoil.

The Dmm₂ facies outcrops in the Lago Sofía section, a 50 m long, 2 m high cliff located on the southern shore of Lago Sofía (**Figure 8.E**). A continuous till belt, previously mapped as a “lateral moraine” by *Sagredo et al. (2011)* despite lacking of a ridge, covers the north-eastern extremity of Cerro Benítez above 170 m a.s.l. The Dcm facies outcrops in the Loicas section, a 1 m high section carved 177 m a.s.l. above a water through (**Figure 8.F**). *Sagredo et al. (2011)* identified a 300 m long ridge culminating 220 m a.s.l., oriented east-west and restricted to the northern extremity of Vega Benítez, as second lateral moraine. However, in the absence of lateral continuity and outcropping till, the ridge more likely reflects the bedrock topography.

- **Glaciofluvial deposits:** Massive, sandy-matrix, clast-supported gravels (Gm) continuously outcrop on the north-eastern side of Cerro Benítez up to 170 m a.s.l. (**Figure 8.G**). The gravels are interpreted as reworked glacial material, slightly reshaped by a short, yet high-energy fluvial transport (**Table 4**). It is possible that the gravels were originally deposited at the ice-margin as a kame terrace, as hypothesised by *Sagredo et al. (2011)*. However, most of the outcropping gravels were likely reworked by lakeshore erosion, at least below 155 m a.s.l.

The Margoni pit was dug in outcropping sand on the northern side of Cerro Benítez, 128 m a.s.l. (**Figure 8.H**). The pit reached the top of a Gm unit downlapped by sand foresets (Sfo) at a depth of 150 cm (**Figure 8.I**). The foresets dip 28° to N020°. In the absence of laterally continuous outcrop, it remains uncertain whether the sand forests were sustained by ice-marginal meltwater or by gullies incised on the northern side of Cerro Benítez.

- **Ice-marginal delta:** *Sagredo et al. (2011)* and *García et al. (2014)* previously mapped an elongate, 1 km long, 600 m wide raised delta at the eastern extremity of Cerro Benítez. The delta culminates at 155 m a.s.l. at its western extremity. The Hongos section is a 300 m long, 20 m high, east-west section located in a gravel pit at the eastern extremity of the delta. The section exposes gravel foresets (Gfo) dipping northwards from 20 to 34° (**Figure 8.J**). The direction of progradation rotates from N355° at the western extremity of the section, to N080° at the eastern extremity. The absence of a connection to a significant catchment area suggests that the delta was sustained by meltwater streams and deposited in a narrow, ice-marginal lake (**Table 4**). Foresets are truncated 130 m a.s.l. and overlain by a pavement of blocks (**Figure 8.K**) interpreted as a lakeshore lag deposit, resulting from a fall of the lake level.

4.2.2. Glaciolacustrine landforms and deposits

- **Lacustrine erosional platform:** Although several authors previously reported the presence of an erosional platform in Cerro Benítez, none has described it in detail (*Caldenius, 1932; Feruglio, 1950; Sagredo et al., 2011; Stern et al., 2011*). The erosional platform continuously surrounds Cerro Benítez and the Lago Sofía valley. It is

carved between 130 and 155 m a.s.l., truncating both bedrock and superficial deposits. Its width ranges from 250 to 800 m on the southern side of Cerro Benítez, and from 50 to 400 m in the Lago Sofía valley.

Palaeoshorelines are marked by horizontal notches, up to 5 m high, on bedrock (**Figure 7.D-G**), and smoother, concave slope discontinuities on superficial deposits (**Figure 7.H-I**). Three main regressive palaeoshorelines are continuously traceable over hundreds of meters, 140, 148 and 155 m a.s.l., respectively (**Figure 2**). Pavements of erratic blocks accumulated by the winnowing of the finer particles and the vertical pressure of lake ice (**Dionne, 1979**) outcrop from the truncated deposits (**Figure 7.G**).

- **Delta:** A 3 km wide raised delta was deposited on the northern side of the Lago Sofía valley up to 155 m a.s.l., at the outlet of the gorge draining the glacial cirque of Cerro Mocho (**Figure 7.K**).
- **Glaciolacustrine deposits:** Located 95 m a.s.l. along the road to Lago Sofía, the 400 m long, 150 cm high Condores section exposes laminated silts and clays (F1) and two embedded allochthonous, magmatic blocks. Considering that the blocks deposited in a lacustrine environments, they are interpreted as dropstones (d) rafted by icebergs from a calving ice margin (**Bennett et al., 1996; Table 1; Figure 8.L**).

4.2.3. Mass wasting landforms and deposits

Paraglacial slopes originate from the relaxation of former ice-contact slopes (**Ballantyne, 2002**). Paraglacial slopes almost continuously surround Cerro Benítez, reaching a maximum height of 50 m on its southern side, above the Mylodon Cave (**Figure 7.L**), and 380 m on its northern side, where the Lago Sofía valley intersects the hinge of the Cerro Benítez anticline (**Figure 7.M**). The catastrophic collapse of conglomerate units (rock slope failure) generates vertical scarps and chaotic, mass wasting deposits composed of metric-sized fragments of conglomerate beds. In contrast, the erosion of the sandstone and mudstone units forms steep slopes, between 20 and 30°. As a result, palaeoshorelines are not preserved where the palaeolake level was in contact with a paraglacial slope.

4.3. Surface exposure ages of erratic blocks

The erratic blocks located between 218 and 512 m, above the lacustrine erosional platform, yielded surface exposure ages ranging from 33.8 ± 1.9 to 37.1 ± 2.4 ka. The surface exposure ages of the erratic blocks located on the lacustrine erosional platform between 136 and 148 m a.s.l. range from 16.8 ± 1.2 to 21.3 ± 1.6 ka. Surface exposure ages within each time interval mutually overlap (**Table 5; Figure 9.A**); hence we did not define outliers and rather assume that the distribution of the surface exposure ages primarily depicts two distinct, rapid surface exposure events: the ice downwasting and lake regression, respectively.

4.4. Chronological model

Assuming that the erratic blocks were exposed as a result of ice downwasting and lake regression, we postulate that each erratic block was exposed after the blocks above and before the blocks below. Hence, we built a relative chronological model where each surface exposure age is ascribed, as prior age, to a surface exposure event, chronologically bracketed by surface exposure ages from upper and lower elevations. The model was completed with a ^{14}C date from the Pantano Dumestre core indicating a minimal date of lake regression, 15.2-15.6 ka cal. BP (**Sagredo et al., 2010**). The minimal dates of ice downwasting and lake regression indicated by the ^{14}C date from the Vega Benítez core (**Sagredo et al., 2011**) and the palaeontological material, respectively (**Table 1**), were not included because they all post-date the surface exposure ages at the same elevation, and thus do not significantly constrain the absolute chronological model.

The absolute difference between the mode of the prior ages and the posterior mode, or *maxima a posteriori* (MAP), of the associated surface exposure events ranges from 0.5 to 3.8 ka, with a mean difference of 2.0 ka. The 95 % high probability density interval (HDPI) of the posterior age distribution of the surface exposure events mostly decreases with elevation,

from a maximum of 14.8 ka to a minimum of 3.1 ka as the ages at lower elevations are closely constrained by a ^{14}C age (Table 6).

The model suggests that ice downwasting from 512 to 218 m a.s.l. occurred between 36.9 (HDPI = 32.6-47.1 ka cal. B2k) and 31.9 ka cal. B2k (HDPI = 25.7-36.1 ka cal. B2k), and the lake regression from 148 to 136 m a.s.l. between 21.7 (HDPI = 18.7-27.7 ka cal. B2k) and 16.9 (HDPI = 15.4-18.5 ka cal. B2k) with a mean rate of 2.5 mm.a⁻¹ (Figure 9.B).

5. Discussion

5.1. Glacial advances in the Última Esperanza fjord

The posterior distribution of the date of ice downwasting, 504 m a.s.l. (MAP = 36.9 ka cal. B2k) fits remarkably well with the surface exposure ages of the erratic blocks from the Dos Lagunas moraine, 34.7 ± 1.9 to 37.8 ± 4.2 ka (Sagredo *et al.*, 2011; Table 2). The ^{10}Be surface exposure ages obtained by García *et al.* (2018) from the Arauco moraine complex are slightly younger (median = 32.7 ka). However, erratic blocks outcropping from glacial deposits are more likely to be subject to exhumation. Hence, their surface exposure ages must be regarded as minimum ages for ice margin retreat (Kaplan *et al.*, 2007; Darvill *et al.*, 2015a). This suggests that the Última Esperanza ice lobe covered the top of Cerro Benítez during the Arauco advance.

The Ballena moraine complex marks the outermost position reached by a glacial advance, west of the Arauco moraine complex. We name this glacial advance the “Ballena advance”. At its maximal extent, the grounded ice margin was located 44 km from the closest present-day ice margin (Balmaceda Glacier), and had retreated some 50 km north-west of the Arauco advance outermost position. García *et al.* (2018) demonstrated from surface exposure dating of erratic blocks that same-order distances separate the outermost position of the Torres del Paine ice lobe during MIS, dated *ca.* 21.5 ka, from the present-day ice margin, the Southern Patagonian Ice Field (45 km), and from its MIS 3 outermost position (30 km). This suggests that the Ballena advance could have occurred in synchronicity with the MIS 2 readvance of the Torres del Paine ice lobe. Hence, the extent of both ice lobes would have been reduced to half between the MIS 3 local LGM and the global LGM. Other outlet glaciers of the Patagonian Ice Sheet experienced a similar trend. For instance, terrestrial cosmogenic nuclide dating of outwash deposits evidenced that the Bahía Inútil-San Sebastián ice lobe, in Tierra del Fuego, retreated by 100 km between MIS 3 and MIS 2 (Darvill *et al.*, 2015b). In the Southern Alps, New Zealand, glaciers reached their maximum extent during MIS 4 and retreated between MIS 3 and MIS 2 (Schaefer *et al.*, 2015; Doughty *et al.*, 2015). Hence, the hypothesis of a glacial readvance mostly restricted to the Última Esperanza fjord during MIS 2 appears consistent with the interpretation of the mid-latitude glacial fluctuations of the Southern Hemisphere through the last glaciation as the result of a hemispheric-scale climate forcing, although its mechanism remains debated (Schaefer *et al.*, 2015; Doughty *et al.*, 2015; Darvill *et al.*, 2016; García *et al.*, 2018; Denton *et al.*, 2021).

5.3. Deglaciation of Cerro Benítez

The MAP of the ice downwasting events provided by the chronological model suggest that the ice lobe locally thinned by *ca.* 300 m in approximately 5,000 years (Figure 10) leaving Cerro Benítez ice-free above at least 218 m a.s.l. Hence, the glacial and glaciofluvial landforms and deposits preserved in Cerro Benítez, including roches moutonnées, subglacial channels, till, glaciofluvial deposits and ice-marginal delta date from the deglaciation that occurred in the aftermath of the Arauco maximum (Figure 11).

The presence of an ice-marginal delta at the eastern extremity of Cerro Benítez suggests that, as the ice surface lowered, the ice lobe separated into two branches occupying the Última Esperanza fjord and the Lago Sofía valley, respectively, leaving Cerro Benítez as a nunatak. The presence of glaciofluvial deposits on the northern side of Cerro Benítez may reflect differences in the sedimentary input with the southern side. In the Lago Sofía valley, local sedimentary inputs from

paraglacial scarps with a height of several hundred meters, and possibly glaciofluvial material from the Cerro Mocho cirque were accumulated at the glacier's surface. In contrast, the ice margin bordering the southern side of Cerro Benítez was in contact with smaller paraglacial scarps, up to several ten meters high, and lacked a significant lateral tributary drainage basin.

5.5. Regression of Lago Consuelo

Following the demise of the Última Esperanza ice lobe, the lithosphere underwent a post-glacial isostatic rebound. Uplift increased westward as a result of the former ice thickness gradient. Hence, the lake basin tilted eastward (Sagredo *et al.*, 2011; Stern *et al.*, 2011). Considering that the lake's outlet was located at the eastern extremity of the lake basin (Figure 1), the tilting of the lake basin caused a forced regression (Teller, 2003). The chronological model suggests that the lake regression from 148 to 136 m a.s.l. occurred with a mean rate of 2.5 mm.a^{-1} . Is this rate suitable for a regressive phase controlled by post-glacial isostatic rebound?

Lange *et al.* (2014) reported from geodetic measurements, parallel to the modelled gradient, an uplift of $2 \pm 6 \text{ mm.a}^{-1}$ in Cerro Benítez and 4 ± 2 to $6 \pm 6 \text{ mm.a}^{-1}$ in Lago Toro, 52 km to the north, representing a mean differential uplift rate of 0.04 to $0.08 \text{ mm.a}^{-1}.\text{km}^{-1}$. Considering that the initial phase of regression occurred at a constant relative outlet lake level, the modelled regression rate of 2.5 mm.a^{-1} in Cerro Benítez represents a differential uplift rate with the lake's outlet, 58 km to the east, of $0.04 \text{ mm.a}^{-1}.\text{km}^{-1}$. This result fits well with the present-day differential uplift rate measured by Lange *et al.* (2014) between Cerro Benítez and Lago Toro. Considering that the present-day elevation of the lake's outlet is 135 m a.s.l., the differential uplift rate must have been negligible since the lake level reached this elevation in Cerro Benítez.

The retreat of the ice margin and the subsequent expansion of Lago Consuelo caused the cessation of ice-marginal sedimentation and the onset of lakeshore erosion and glaciolacustrine sedimentation. Previous authors assumed waves as the main erosional agent on the platform (Feruglio, 1950; Sagredo *et al.*, 2011; Stern *et al.*, 2011). In contrast, several authors have proposed frost-shattering as a major erosional process on periglacial lakeshores with waves playing a secondary role as a transporting agent of debris only (Matthews *et al.*, 1986; Dawson *et al.*, 1987; Shakesby and Matthews, 1987; Ryder, 1991; Aarseth and Fossen, 2004). Matthews *et al.* (1986) proposed a model of development for lacustrine erosional platform involving the triple action of segregation ice, lake water migration and lake ice. As the freezing interval expands into the ground, the growth of segregation ice causes the migration of lake water through the bedrock toward the freezing plane. Maximal water supply at the interface between lake and bedrock promotes optimal frost-shattering. A planation surface therefore develops within the freezing depth interval. Frost-shattered debris are removed by drifting lake ice when the lake's surface starts to thaw, and eventually by waves. During the global LGM, permafrost covered Patagonia south of 48°S (Trombotto, 2011). Hence, growth of segregation ice must have occurred annually within the active layer of the permafrost as the ground freezing front reached the lake water freezing front (Figure 12). Mean erosion rates of two Holocene periglacial lacustrine platforms carved on gabbros have been estimated at 2.6 to 4.4 and 2.2 cm.a^{-1} , respectively (Matthews *et al.*, 1986; Shakesby and Matthews, 1987). Chronological modelling predicts that lake regression from 148 to 140 m a.s.l. most probably occurred in 4,200 years. Within such a time interval, erosional rates estimated by Matthews *et al.* (1986) and Shakesby and Matthews (1987) would produce a 92 to 185 m wide platform. These dimensions fits well with the actual distance separating the 148 from the 140 m a.s.l. palaeoshorelines which ranges from 50 m, in the Mylodon Labyrinth, to 200 m, on the south-western side of Cerro Benítez. The lateral variability of the platform width might be explained by lithological contrasts. Indeed, erosion rate is expected higher on sandstone and mudstone than conglomerate, considering that sandstone and mudstone produce are more finely bedded and therefore, less resistant to frost-shattering.

The lake regression to 77 m a.s.l. was caused by the drainage reversal to the Magellan lake (Stern *et al.*, 2011; Kilian *et al.*, 2013). Chronological modelling suggests a minimum date of lake regression from 77 m a.s.l. at ca. 15.4 ka (HDPI = 15.0-15.7 ka). Hence, the regression from 136 to 77 m a.s.l. must have occurred in less than 1,500 years, in agreement with the rapid fall of the lake level following a drainage reversal.

Previous authors (Stern *et al.*, 2011; Villaviciencio *et al.*, 2016) hypothesised that the onset of the colonisation of Cerro Benítez by megafauna occurred as Cerro Benítez connected to the mainland. This implies that the lake level had already dropped below 115 m, according to our DSM. However, chronological modelling indicates that the MAP of the lake regression from 136 m a.s.l. occurred at 16.9 ka cal. B2k, ca. 1,000 years after the earliest evidence of megafaunal presence in Cerro Benítez at 17.9-18.3 ka cal. BP. At that time, the lake level was most probably between 140 and 143 m a.s.l. (Figure 9.C). In this case, megafauna would have colonised Cerro Benítez as an island, either by swimming across the lake or walking on lake ice. Considering that the HDPI of the lake regression event from 136 m a.s.l. completely overlaps the 2σ probability interval of the earliest ^{14}C age of megafaunal material, neither of the two hypotheses can be ruled out from chronological modelling only. Alternatively, the answer could arise in the future from a quantitative description of the faunal assemblages through the cave sedimentary sequences coupled with a robust depositional age model, which could help to detect faunal changes reflecting changes in the accessibility of the caves.

6. Conclusion

We propose a detailed chronological reconstruction of the demise of the Patagonian Ice Sheet in the area of Cerro Benítez and the regression of Lago Consuelo summarised in Table 7 and Figure 13. This reconstruction relies on chronological modelling based on ^{10}Be surface exposure dating. Modelled ages must be interpreted cautiously, considering that they are calculated based on a hypothetical relative chronology postulating that the surface exposure ages primarily date the lowering of the glacier's surface and emergence of erratic blocks, respectively. Despite this initial uncertainty, our chronological model is independently consistent with other sets of surface exposure and ^{14}C ages provided by previous authors, the rate of local uplift, and erosion rate of Holocene lacustrine erosional platforms. These results confirm that the use of chronological modelling to unravel sets of absolute dates with high uncertainties, but robust relative chronological relations, can enhance the chronological reconstruction of deglaciation (Thorndycraft *et al.*, 2019).

Chronological modelling suggests that Cerro Benítez was totally covered by the Última Esperanza ice lobe until 36.9 ka. The ice lobe then locally thinned by 300 m in 5,000 years, leaving Cerro Benítez as a nunatak above 218 m a.s.l. Identification a new moraine complex, the Ballena moraine complex, indicates that the ice margin subsequently readvanced to 5 km east of Cerro Benítez, within 50 km of its MIS 3 outermost position. This confirms that Patagonian Ice Sheet experienced a major decrease in volume prior to the global LGM, as well as other mid-latitude outlet glaciers of the Southern Hemisphere, and in agreement with the conclusions of Davies *et al.* (2020) and Denton *et al.* (2021).

The final retreat of the Última Esperanza ice lobe involved a rapid transition from a subglacial to a glaciolacustrine environment between 31.9 and 21.7 ka. The cessation of the ice-marginal sedimentary inputs exposed glacial and glaciofluvial deposits to lakeshore erosion. Periglacial conditions promoted the development of a lacustrine erosional platform on bedrock and superficial deposits between 130 and 155 m a.s.l. The lake regression occurred in two distinct phases. The first phase was slow (2.5 mm.a^{-1}) and was controlled by the tilting of the lake basin due to differential isostatic rebound between Cerro Benítez and the

lake's outlet. The earliest evidence of megafaunal presence in Cerro Benítez, at 17.9-18.3 ka cal. BP, suggests megafaunal colonisation of Cerro Benítez as an island, as the erosional platform isostatically emerged with the caves and rock shelters. The second phase of lake regression was triggered by the drainage reversal of Lago Consuelo to the Magellan lake and occurred between 16.9 and 15.4 ka, some 4,000 years before the earliest evidence of human presence in the area.

Acknowledgments

This work was funded by the Chilean FONDECYT (projects 1150845 and 1180272), the French CNRS (PICS GEOCEBE), the Istanbul Technical University (research project TGA-2017-40610), a PhD studentship from the university of Rouen awarded to I.G. and a mobility grant from the French Institut des Amériques awarded to I.G. Pléiades satellite images were acquired from Airbus DS Geo via Dinamis. We acknowledge Valentina García Huidobro Mery and Ylara Vela-Ruiz Figueroa, Florentina Pérez Martín, Erik Lukoviek and José Díaz Tavie for their assistance on the field, Céline Colange and Olivier Gillet for their assistance to collect and process the satellite images and Joël Rodet for our scientific exchanges. We gratefully thank the CONAF, Ciro Barría, Alejandra Olivares, Rodrigo Rodríguez and the other guards of the Mylodon Cave Natural Monument for their hospitality and assistance during our fieldwork, and Ernesto Helmer, Francisca Helmer, Jorge Canales Helmer and Mario Margoni for their permission to work on their properties. We thank Juan-Luis Garcia and Varyl Thorndycraft for their helpful review.

References

1. Aarseth, I., Fossen, H., 2004. A Holocene lacustrine rock platform around Storavatnet, Osterøy, western Norway. *The Holocene*, 14(4), 589-596.
2. Anderson, J., Shipp, S., Lowe, A., Wellner, J., Mosola, A., 2002. The Antarctic Ice Sheet during the LGM and its subsequent retreat history. *Quaternary Science Reviews*, 21, 49-70.
3. Balco, G., Stone, J. O., Lifton, N. A., Dunai, T. J., 2008. A complete and easily accessible means of calculating surface exposure ages or erosion rates from ^{10}Be and ^{26}Al measurements. *Quaternary Geochronology*, 3, 174-195.
4. Ballantyne, C. K., 2002. Paraglacial geomorphology. *Quaternary Science Reviews*, 21(18–19), 1935-2017.
5. Bendle, J.M., Palmer, A.P., Thorndycraft, V.R., Matthews, I.P., 2017b. High-resolution chronology for deglaciation of the Patagonian ice sheet at Lago Buenos Aires (46.5° S) revealed through varve chronology and Bayesian age modelling. *Quat. Sc. Rev.*, 177, 314-338.
6. Bendle, J.M., Thorndycraft, V.R., Palmer, A.P., 2017a. The glacial geomorphology of the Lago Buenos Aires and Lago Pueyrredon ice lobes of central Patagonia. *J. Maps* 13, 654-673.
7. Boex, J., Fogwill, C., Harrison, S., Glasser, N. F., Hein, A., Schnabel, C., Xu, S., 2013. Rapid thinning of the late Pleistocene Patagonian Ice Sheet followed migration of the Southern Westerlies. *Scientific Reports* 3, 2118.
8. Borchers, B., Marrero, S., Balco, G., Caffee, M., Goehring, B., Lifton, N., Nishiizumi, K., Phillips, F., Schaefer, J., Stone, J., 2016. Geological calibration of spallation production rates in the CRONUS-Earth project. *Quat. Geochronol.* 31, 188-198.
9. Brodzikowski, K., van Loon, A. J., 1987. Glacigenic sediments. *Earth Science Reviews*, 24, 297-381.

10. Caldenius, C., 1932. Las glaciaciones cuaternarias en Patagonia y Tierra del Fuego. *Geografiska Annaler*, 14, 1–164.
11. Chandler, B. M. P., Lovell, H., Boston, C. M., Lukas, S., Barr, I. D., Benediktsson, Í. Ö., Benn, D. I., Clark, C. D., Darvill, C. M., Evans, D. J. A., Ewertowski, M. W., Loibl, D., Margold, M., Otto, J.-C., Roberts, D. H., Stokes, C. R., Storrar, R. D., Stroeven, A. P., 2018. Glacial geomorphological mapping: a review of approaches and frameworks for best practice. *Earth Sci. Rev.*, 185, 806-846.
12. Chiverrell, R., Foster, G., Thomas, G., Marshall, P., Hamilton, W., 2009. Robust chronologies for landform development. *Earth Surface Processes and Landforms*, 34, 319-328.
13. Darvill, C. M., Bentley M. J., Stokes C.R., 2015a. Geomorphology and weathering characteristics of erratic boulder trains on Tierra del Fuego, southernmost South America: implications for dating of glacial deposits. *Geomorphology*, 228, 382-397.
14. Darvill, C. M., Bentley, M. J., Stokes, C. R., Hein, A. S., Rodes, A., 2015b. Extensive MIS 3 glaciation in southernmost Patagonia revealed by cosmogenic nuclide dating of outwash sediments. *Earth Planet. Sci. Lett.*, 429, 157-169.
15. Darvill, C. M., Bentley, M. J., Stokes, C. R., Shulmeister, J., 2016. The timing and cause of glacial advances in the southern mid-latitudes during the last glacial cycle based on a synthesis of exposure ages from Patagonia and New Zealand. *Quat. Sci. Rev.*, 149, 200-214.
16. Darvill, C. M., Stokes, C.R., Bentley, M. J., Lovell, H., 2014. A glacial geomorphological map of the southernmost ice lobes of Patagonia: the Bahia Inutil-San Sebastian, Magellan, Otway, Skyring and Rio Gallegos lobes. *J. Maps*, 10, 500-520.
17. Davies, B. 2021. Dating Glacial Landforms II: Radiometric techniques. In: Haritashya, U. (Ed.), *Cryospheric Geomorphology*. Treatise on Geomorphology, 2nd Edition, Elsevier.
18. Davies, B. J., Darvill, C. M., Lovell, H., Bendle, J. M., Dowdeswell, J. A., Fabel, D., García, J.-L., Geiger, A., Glasser, N. F., Gheorghiu, D. M., Harrison, S., Hein, A. S., Kaplan, M. R., Martin, J. R. V., Mendelova, M., Palmer, A., Pelto, M., Rodés, Á., Sagredo, E. A., Smedley, R. K., Smellie, J. L., Thorndycraft, V. R., 2020. The evolution of the Patagonian Ice Sheet from 35 ka to the present day (PATICE). *Earth-Science Reviews*, 204, 1-77.
19. Davies, B. J., Thorndycraft, V. R., Fabel, D., Martin, J. R. V., 2018. Asynchronous glacier dynamics during the Antarctic Cold Reversal in central Patagonia. *Quat. Sci. Rev.*, 200, 287-312.
20. Davies, B., Glasser, N., 2012. Accelerating shrinkage of Patagonian glaciers from the Little Ice Age (~AD 1870) to 2011. *Journal of Glaciology*, 58(212), 1063-1084.
21. Dawson, A. G., Matthews, J. A., Shakesby, R. A., 1987. Rock platform erosion on periglacial shores: a modern analogue for Pleistocene rock platforms in Britain. In: Boardman, J. (Ed.), *Periglacial processes and landforms in Britain and Ireland*, 173-182.
22. Denton, G. H., Putnam, A. E., Russell, J. L., Barrell, D. J. A., Schaefer, J. M., Kaplan, M. R., Strand, P. D., 2021. The Zealandia Switch: Ice age climate shifts viewed from Southern Hemisphere moraines. *Quaternary Science Reviews*, 257, 106771.
23. Dionne, J.-C., 1979. Ice Action in the Lacustrine Environment. A Review With Particular Reference to Subarctic Quebec, Canada. *Earth-Science Reviews*, 15, 185-212.

24. Doughty, A. M., Schaefer, J. M., Putnam, A. E., Denton, G. H., Kaplan, M. R., Barrell, D. J. A., Andersen, B. G., Finkel, R. C., Schwartz, R., 2015. Mismatch of glacier extent and summer insolation in Southern Hemisphere mid-latitudes. *Geology*, 43(5), 407-410.
25. Evans, D. J. A. (Ed.), *Glacial Landscapes*. Hodder Arnold, London, 544 p.
26. Evans, D. J. A., Benn, D. I., 2004. Facies description and the logging of sedimentary exposures. In: Evans, D. J. A., Benn, D. I. (Eds), *A Practical Guide to the Study of Glacial Sediments*, 11-51.
27. Evans, D. J. A., Phillips, E. R., Hiemstra, J. F., Auton, C. A., 2006. Subglacial till: Formation, sedimentary characteristics and classification. *Earth-Science Reviews*, 78, 115-176.
28. Fabel, D., Small, D., Miguens-Rodriguez, M., Freeman, S. P. H. T., 2010. Cosmogenic nuclide exposure ages from the 'Parallel Roads' of Glen Roy, Scotland. *J. Quat. Sci.*, 25, 597-603.
29. Feruglio, E., 1950. Descripción geológica de la Patagonia. Tomo III. Dirección General de Yacimientos Petrolíferos Fiscales, Buenos Aires, 207-218.
30. Fosdick, J., Romans, B. W., Fildani, A., Bernhardt, A., Calderón, M., Graham, S. A., 2011. Kinematic evolution of the Patagonian retroarc fold-and-thrust belt and Magallanes foreland basin, Chile and Argentina, 51°30'S. *Geological Society of America Bulletin*, 123, 1679-1698.
31. Fountain, A. G., Walder, J. S., 1998. Water flow through temperate glaciers. *Review of Geophysics*, 36(3), 299-328.
32. García, J. L., Hall, B. L., Kaplan, M. R., Vega, R. M., Strelin, J. A., 2014. Glacial geomorphology of the Torres del Paine region (southern Patagonia): implications for glaciation, deglaciation and paleolake history. *Geomorphology*, 204, 599-616.
33. García, J. L., Hein, A. S., Binnie, S. A., Gomez, G. A., Gonzalez, M. A., Dunai, T. J., 2018. The MIS 3 maximum of the Torres del Paine and Última Esperanza ice lobes in Patagonia and the pacing of southern mountain glaciation. *Quaternary Science Reviews*, 185, 9-26.
34. Genuite, K., Delannoy, J. J., Bahain, J. J., Gresse, M., Jaillet, S., Philippe, A., Pons-Branchu, E., Revil, A., Voinchet, P., 2021. Dating the landscape evolution around the Chauvet-Pont d'Arc cave. *Scientific Reports* 11, 8944.
35. Gersonde, R., Crosta, X., Abelmann, A., Armand, L., 2005. Sea-surface temperature and sea ice distribution of the Southern Ocean at the EPILOG Last Glacial Maximum—a circum-Antarctic view based on siliceous microfossil records. *Quaternary Science Reviews*, 24(7-9), 869-896.
36. Glasser, N. F., Bennett, M. R., 2004. Glacial erosional landforms: origins and significance for palaeoglaciology. *Progress in Physical Geography: Earth and Environment*, 28(1), 43-75.
37. Glasser, N. F., Hambrey, M. J. 1998. Subglacial meltwater channels at Thurstaston Hill, Wirral and their significance for Late Devensian ice sheet dynamics. *Proceedings of the Geologists' Association*, 109, 139-148.
38. Glasser, N. F., Jansson, K. N., Harrison, S., Klemen, J., 2008. The glacial geomorphology and Pleistocene history of Southern South America between 38°S and 56°S. *Quaternary Science Reviews*, 27, 365-390.
39. Glasser, N., Jansson, K., 2008. The Glacial Map of southern South America. *Journal of Maps*, 4, 175-196.

40. Gosse, J. C., Phillips, F. M., 2001. Terrestrial in situ cosmogenic nuclides: Theory and application. *Quaternary Science Reviews*, 20, 1475-1560.
41. Greenwood, S., Clark, C., Hughes, A., 2007. Formalising an inversion methodology for reconstructing ice-sheet retreat patterns from meltwater channels: Application to the British Ice Sheet. *Journal of Quaternary Science*, 22, 637-645.
42. Hauthal, R. 1899. I: Reseña de los hallazgos en las cavernas de Última Esperanza. In: Hauthal, R., Roth, S., Lehmann-Nitsche, R. (Eds.), *El mamífero misterioso de la Patagonia "Gryotherium domesticum"*. *Revista del Museo de La Plata*, 9, 411-420.
43. Hogg, A., Heaton, T., Hua, Q., Palmer, J., Turney, C., Southon, J., Bayliss, A., Blackwell, P.G., Boswijk, G., Ramsey, C. B., Pearson, C., Petchey, F., Reimer, P., Reimer, R., Wacker, L., 2020. SHCal20 Southern Hemisphere Calibration, 0-55,000 Years cal BP. *Radiocarbon*, 62(4), 759-778.
44. Hubbard, S. M., Romans, B. W., Graham, S. A., 2007. An outcrop example of large-scale conglomeratic intrusions sourced from deep-water channel deposits, Cerro Toro Formation, Magallanes Basin, southern Chile. In: Hurst, A., Cartwright, J. (Eds), *Sand Injectites: Implications for Hydrocarbon Exploration and Production*, American Association of Petroleum Geologists Bulletin Memoir, 87, 199-207.
45. Hubbard, S. M., Romans, B. W., Graham, S. A., 2008. Deep-water foreland basin deposits of the Cerro Toro Formation, Magallanes Basin, Chile: architectural elements of a sinuous basin axial channel belt. *Sedimentology*, 55, 1333-1359.
46. Kaplan M. R., Ackert, R. P., Singer, B. S., Douglass, D. C., Kurz, M. D., 2004. Cosmogenic nuclide chronology of millennial-scale glacial advances during O-isotope Stage 2 in Patagonia. *Geological Society of America Bulletin* 116: 308-321.
47. Kaplan, M. R., Coronato, A., Hulton, N. R. J., Rabassa, J. O., Stone, J. O., Kubik, P. W., 2007. Cosmogenic nuclide measurements in southernmost South America and implications for landscape change. *Geomorphology*, 87, 284-301.
48. Kaplan, M. R., Strelin, J. A., Schaefer, J. M., Denton, G. H., Finkel, R. C., Schwartz, R., Putnam, A.E., Vandergoes, M. J., Goehring, B. M., Travis, S. G., 2011. In-situ cosmogenic ^{10}Be production rate at Lago Argentino, Patagonia: implications for late-glacial climate chronology. *Earth Planet Sci. Lett.* 309, 21-32.
49. Kilian, R., Baeza, O., Breuer, S., Rios, F., Arz, H., Lamy, F., Wirtz, J., Baque, D., Korf, P., Kremer, K., Ríos, C., Mutschke, E., Simon, M., De Pol-Holz, R., Arevalo, M., Wörner, G., Schneider, C., Casassa, G., 2013. Late Glacial and Holocene Paleogeographical and Paleoeological Evolution of the Seno Skyring and Otway Fjord Systems in the Magellan Region. *An. Inst. Patagonia*, 41, 5-26.
50. Korschinek, G., Bergmaier, A., Faestermann, T., Gerstmann, U. C., Knie, K., Rugel, G., Wallner, A., Dillmann, I., Dollinger, G., Lierse von Gostomski, C., Kossert, K., Maiti, M., Poutivtsev, M., Remmert, A., 2010. A new value for the half-life of ^{10}Be by Heavy-Ion Elastic Recoil Detection and liquid scintillation counting. *Nuclear Instruments and Methods in Physics Research Section B: Beam Interactions with Materials and Atoms*, 268(2), 187-191.
51. Labarca, E. R., Prieto, I. A., 2009. Osteometría de *Vicugna vicugna* Molina, 1782 en el Pleistoceno final de Patagonia meridional chilena: Implicancias paleoecológicas y biogeográficas. *Rev. Mus. Antropol.*, 2, 127-140.

52. Lange, H., Casassa, G., Ivins, E., Schröder, L., Fritsche, M., Richter, A., Groh, A., Dietrich, R., 2014. Observed crustal uplift near the Southern Patagonian Icefield constrains improved viscoelastic Earth models. *Geophysical Research Letters*, 41, 10.1002/2013GL058419.
53. Lanos, P., Dufresne, P., 2019. ChronoModel version 2.0 User manual. 84 p.
54. Lanos, P., Philippe, A., 2015. Hierarchical Bayesian modeling for combining Dates in archaeological context. 17 p.
55. Lifton, N., Sato, T., Dunai, T. J., 2014. Scaling in situ cosmogenic nuclide production rates using analytical approximations to atmospheric cosmic-ray fluxes. *Earth and Planetary Science Letters*, 386, 149-160.
56. Martin, F. M., Borrero, L. A., 2017. Climate change, availability of territory, and Late Pleistocene human exploration of Ultima Esperanza, South Chile. *Quaternary International*, 428, 86-95.
57. Martin, F. M., Borrero, L. A., Prevosti, F. J., Todisco, D., Girault, I., San Román, M., Morello, F., García-Huidobro, V., Stern, Charles, 2020. Late Pleistocene Faunal Evidences at Cerro Benitez, Ultima Esperanza, Chile: Colonization, Occupation and Extinction. Submitted.
58. Martin, F. M., San Román, M., Morello, F., Todisco, D., Prevosti, F. J., Borrero, L. A., 2013. Land of the ground sloths: recent research at Cueva Chica, Ultima Esperanza, Chile. *Quaternary International*, 305, 56-66
59. Martin, F., Todisco, D., Rodet, J., San Roman, M., Morello, F., Prevosti, F., Stern, C., Borrero, L.A., 2015. Nuevas excavaciones en Cueva del Medio. procesos de formacion de la cueva y avances en los estudios de interaccion entre cazadores recolectores y fauna extinta (Pleistoceno final, Patagonia meridional). *Magallania*, 43, 165-189.
60. Martinic, M., 1996. La Cueva del Milodón: historia de los hallazgos y otros sucesos. Relación de los estudios realizados a lo largo de un siglo (1895-1995). *An. Inst. Patagonia*, 24, 43-80.
61. Matthews, J. A., Dawson, A. G., Shakesby, R. A., 1986. Lake shoreline development, frost weathering and rock platform erosion in an alpine periglacial environment, Jotunheimen, southern Norway. *Boreas*, 15(1), 33-50.
62. Mix, A. C., Bard, E., Schneider, R., 2001. Environmental processes of the ice age: land, oceans, glaciers (EPILOG). *Quaternary Science Reviews* 20, 627-657.
63. Moreno, F. P., 1899. Explorations in Patagonia. *The Geographical Journal*, 14(3), 241-269.
64. Nami, H. G., 1985-1986. Excavación arqueológica y hallazgo de una punta cola de pescado Fell 1 en la cueva del Medio. *An. Inst. Patagonia*, 16, 103-109.
65. Nami, H. G., Nakamura, T., 1995. Cronología radiocarbonica con AMS sobre muestras de huesos procedentes del sitio Cueva del Medio (Ultima Esperanza, Chile). *An. Inst. Patagonia*, 32, 125-133.
66. Nordenskjöld, O., 1899. Wissenschaftliche Ergebnisse der Schwedischen Expedition nach den Magellansländern 1895-1897. Bd. I. Geologie, Geographie und Anthropologie. P.A. Norstedt & söner, 256 p.
67. Prieto, A., 1991. Cazadores tempranos y tardios en Cueva del Lago Sofía 1. *An. Inst. Patagonia* 20, 75-99.
68. Romans, B. W., Fildani, A., Hubbard, S. M., Covault, J. A., Fosdick, J. C., Graham, S. A., 2011. Evolution of deep-water stratigraphic architecture, Magallanes Basin, Chile. *Marine and Petroleum Geology*, 28, 612-628.
69. Ryder, J. M., 1991. Geomorphological Processes Associated with an Ice-Marginal Lake at Bridge Glacier, British Columbia. *Géographie physique et Quaternaire*, 45(1), 35-44.

70. Sagredo, E. A., Moreno, P. I., Villa-Martinez, R., Kaplan, M. R., Kubik, P. W., Stern, C. R., 2011. Fluctuations of the Última Esperanza ice lobe (52°S), Chilean Patagonia, during the last glacial maximum and termination. *Geomorphology*, 125, 92-108.
71. Sawagaki, T., Hirakawa, K., 1997. Erosion of bedrock by subglacial meltwater, Soya Coast, East Antarctica. *Geografiska Annaler. Series A, Physical Geography*, 79(4), 223-238.
72. Schaefer, J. M., Putnam, A. E., Denton, G. H., Kaplan, M. R., Birkel, S., Doughty, A. M., Kelley, S., Barrell, D. J. A., Finkel, R. C., Winckler, G., Anderson, R. F., Ninneman, U. S., Barker, S., Schwartz, R., Andersen, B. G., Schluechter, C., 2015. The Southern Glacial Maximum 65,000 years ago and its Unfinished Termination. *Quaternary Science Reviews*, 114, 52-60.
73. Shakesby, R. A., Matthews, J. A., 1987. Frost weathering and rock platform erosion on periglacial lake shorelines: a test of a hypothesis. *Norsk Geologisk Tidsskrift*, 67, 197-203.
74. Solari, M., Le Roux, J., Hervé, F., Airo, A., Calderón, M., 2012. Evolution of the Great Tehuelche Paleolake in the Torres del Paine National Park of Chilean Patagonia during the Last Glacial Maximum and Holocene. *Andean Geology*, 39, 1-21.
75. Steele, J., Politis, G., 2009. AMS 14C dating of early human occupation of southern South America. *J. Arch. Sci.*, 36, 419-442.
76. Stern, C. R., Moreno, P. I., Villa-Martinez, R., Sagredo, E. A., Prieto, A., Labarca, R., 2011. Evolution of ice-dammed proglacial lakes in Última Esperanza, Chile: implications from the late-glacial R1 eruption of Reclús volcano, Andean Austral Volcanic Zone. *Andean Geology*, 38(1), 82-97.
77. Teller, J. T., 2003. Subaquatic landsystems: large proglacial lakes. In: Evans, D. J. A. (Ed.), *Glacial Landsystems*. Hodder Arnold, London, 348-371.
78. Thorndycraft, V. R., Bendle, J. M., Benito, G., Davies, B. J., Sancho, C., Palmer, A. P., Fabel, D., Medialdea, A., Martin, J. R. V., 2019. Glacial lake evolution and Atlantic-Pacific drainage reversals during deglaciation of the Patagonian Ice Sheet. *Quat. Sci. Rev.*, 203, 102-127.
79. Todisco, D., Rodet, J., Nehme, C., Martin, F., Borrero, L. A., 2018. Les cavités du Cerro Benitez (Patagonie, Chili). Hypothèses génétiques glacio-karstiques. *Karstologia*, 67, 31-42.
80. Trombotto, D., 2011. Geocryology of Southern South America. In: Rabassa, J. (Ed.), *Late Cenozoic of Patagonia and Tierra del Fuego. Developments in Quaternary Sciences*, 11, Elsevier, Amsterdam, 255-268.
81. van der Meer, J. J. M., Menzies, J., Rose, J., 2003. Subglacial till: the deforming glacier bed. *Quaternary Science Reviews*, 22, 1659-1685.
82. Bennett, M., Doyle, P., Mather, A., 1996. Dropstones: Their origin and significance. *Palaeogeography, Palaeoclimatology, Palaeoecology*, 121, 331-339.
83. Empeaire, G., Laming, A., 1954. La grotte du Mylodon (Patagonie occidentale). *Journal de la Société des Américanistes*, 43, 173-206.
84. Borrero, L. A., Martin, F., 2012. Taphonomic observations on ground sloth bone and dung from Cueva del Milodón, Última Esperanza, Chile: 100 years of research history. *Quaternary International*, 278, 3-11.

Figure 1: Geomorphological map of the Última Esperanza fjord at the scale of 1:500,000. PIS: Patagonian Ice Sheet. NPIF: Northern Patagonian Ice Field. SPIF: Southern Patagonian Ice Field. CDIF: Cordillera Darwin Ice Field. a: Lago Dorotea core; b: Vega Benítez core; c: Eberhard core; d: Dorotea Pits section; e: Pantano Laurita core; f: Dorotea Crossroad section; g: Dumestre section; h: Antonio Varas section; i: Pantano Dumestre core; j: Lago Arauco core; k: Lago Pintito core. A-F: areas mapped at the scale of 1:50,000 in Figure 3.

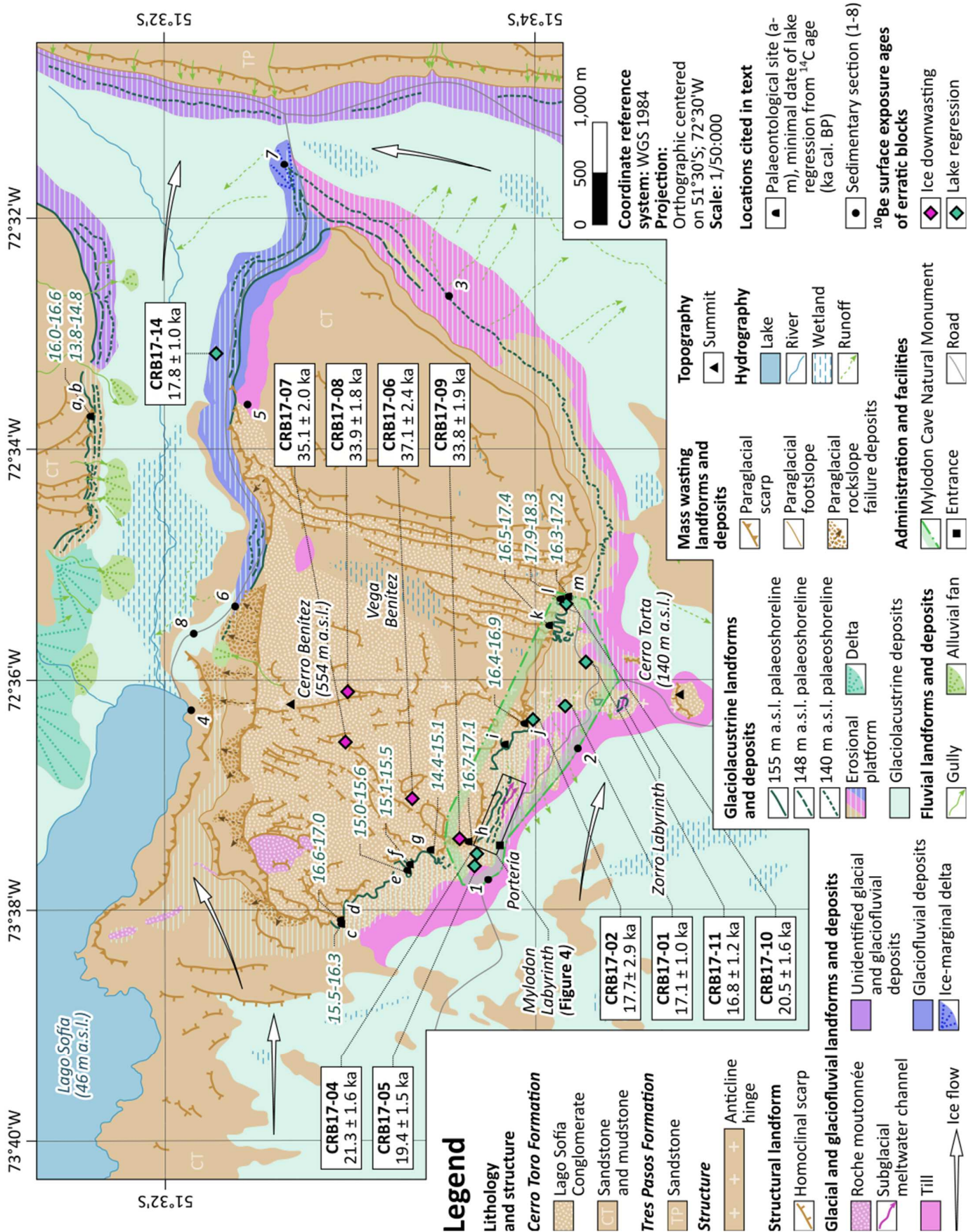
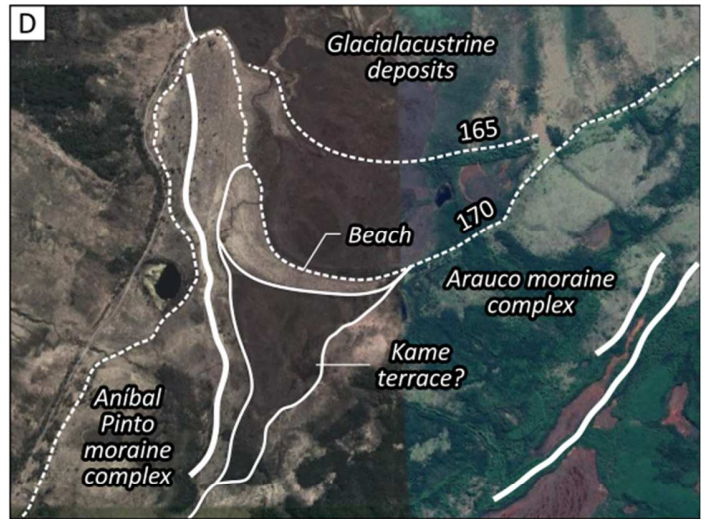


Figure 2: Geomorphological map of Cerro Benítez at the scale of 1:50,000. a: Cueva Lago Sofía 1; b: Cueva Lago Sofía 4; c: Cueva de la Ventana; d: Cueva Escondida; e: Alero Dos Herraduras; f: Alero Los Bloques; g: Alero Norte; h: Cueva del Milodón; i: Alero Las Ovejas Muertas; j: Cueva del Medio; k: Cueva Nordenskjöld; l: Cueva Chica; m: Cueva Ciro. 1: Portería section; 2: Silla del Diablo section; 3: Los Caranchos pit; 4: Lago Sofía section; 5: Las Loicas section; 6: Margoni pit; 7: Los Hongos section. 8: Los Condores section.



Legend

-  Superficial deposit limit
-  Moraine ridge
-  Palaeoshoreline (m a.s.l.)



Satellite image: Google Earth imagery (© 2021 CNES/Airbus: A, B, C, D, E, F; © 2021 Maxar Technologies: D, F; © 2021 Google: D, F)
Coordinate reference system: WGS 1984

Projection: Orthographic centered on 51°30'S; 72°30'W
Scale: 1:50,000

Figure 3: Glacial and glaciolacustrine landforms and deposits of the Lago Consuelo area. **A:** lakeshore spit and outlet channel, 135 m a.s.l. **B:** lakeshore barrier, 138 m a.s.l., and beach, 142 m a.s.l. **C:** delta, 145 m a.s.l. **D:** beach, 170 m a.s.l. **E:** north-western extremity of the Ballena moraine complex. **F:** southern extremity of the Ballena moraine complex.

Legend

-  Lago Sofia Conglomerate
-  Fracture
-  Subglacial till
-  Subglacial meltwater channel
-  Subglacial meltwater channel bank
-  Subglacial meltwater flow
-  Palaeoshoreline (m a.s.l.)
-  Erosional platform
-  Paraglacial scarp
-  Building
-  Trail

Coordinate reference system: WGS 1984
Projection: Orthographic centered on 51°30'S; 72°30'W
Scale: 1:5,000

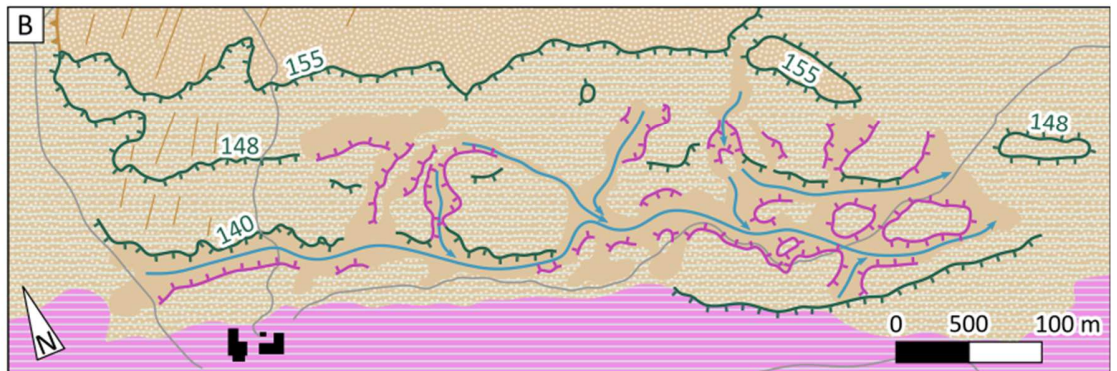
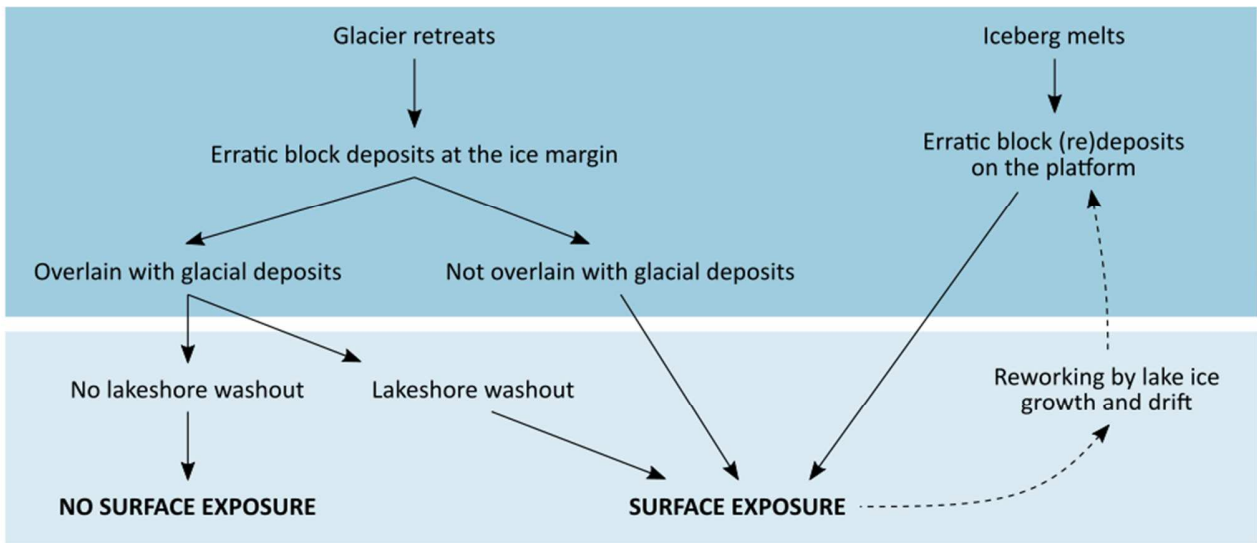
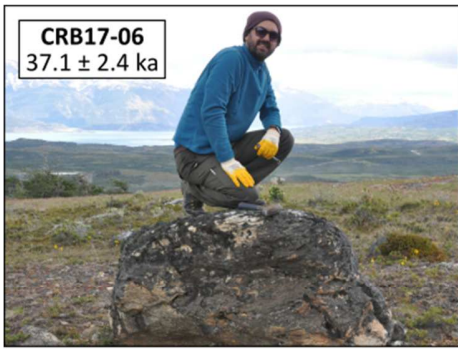


Figure 4: Geomorphological map of the Mylodon Labyrinth at the scale of 1:5,000. **A:** orthorectified aerial drone photography cover. **B:** geomorphological interpretation highlighting the intricate arrangement of subglacial meltwater channels and lacustrine palaeoshorelines.



Deep subaqueous environment (> 1.6 m deep)
 Shallow subaqueous (< 1.6 m deep) to aerial environment

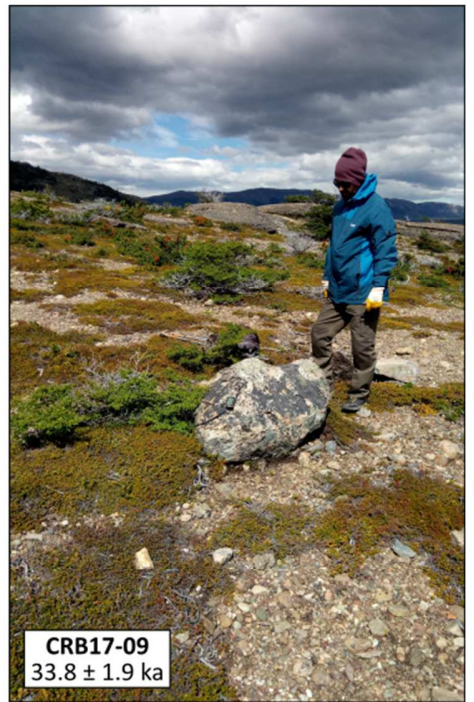
Figure 5: Hypothetical paths of depositional and post-depositional history of the erratic blocks located on the lacustrine erosional platform prior to surface exposure.



CRB17-06
37.1 ± 2.4 ka



CRB17-07
35.1 ± 2.0 ka



CRB17-09
33.8 ± 1.9 ka



CRB17-08
33.9 ± 1.8 ka



CRB17-04
21.3 ± 1.6 ka



CRB17-10
20.5 ± 1.6 ka



CRB17-05
19.4 ± 1.5 ka



CRB17-14
17.8 ± 1.0 ka



CRB17-02
17.7 ± 2.9 ka



CRB17-01
17.1 ± 1.0 ka



CRB17-11
16.8 ± 1.2 ka

Figure 6: Erratic blocks sampled in Cerro Benítez and their ^{10}Be surface exposure ages.

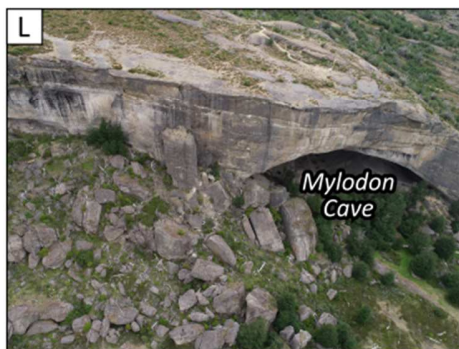
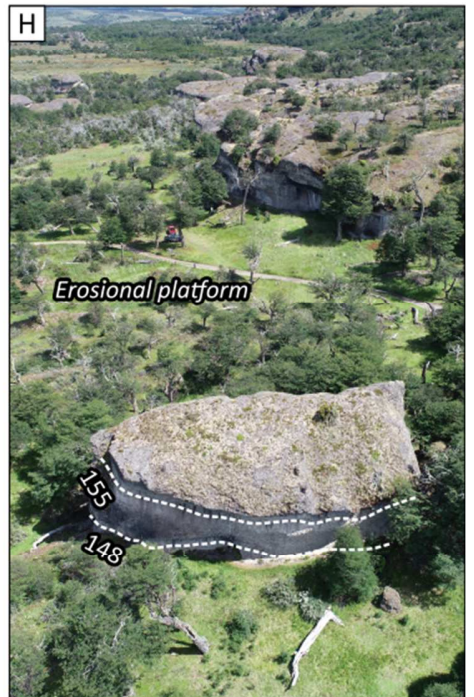
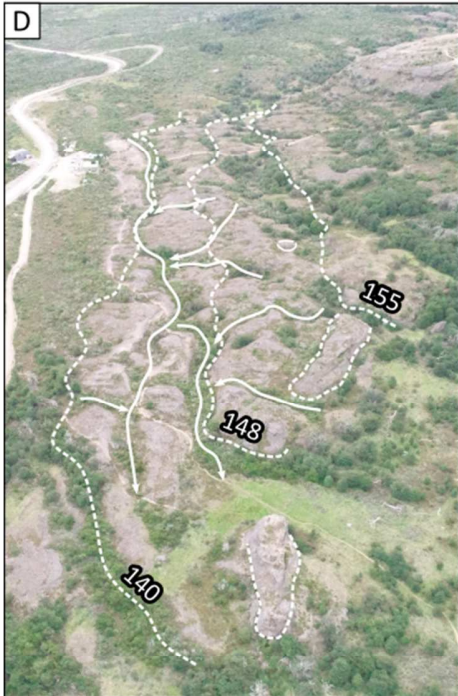
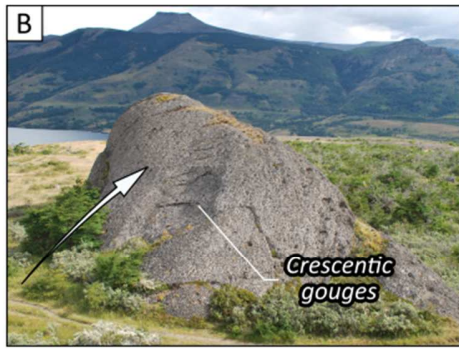


Figure 7: Landforms of Cerro Benítez and the Lago Sofía valley. **A:** roche moutonnée carved by a westward ice flow on a westward-dipping conglomerate unit, *ca.* 300 m a.s.l. **B:** roche moutonnée carved by a N020 ice flow on a discordant conglomerate injectite, northwestern side of Cerro Benítez, 150 m a.s.l. **C:** roche moutonnée carved by an eastward ice flow on a westward-dipping conglomerate unit, southern side of Cerro Benítez, 155 m a.s.l. **D:** oblique aerial view of the Mylodon Labyrinth. **E:** oblique aerial view of the Zorro Labyrinth. **F:** lacustrine notch near Cueva del Medio, 155 m a.s.l. **G:** oblique aerial view of lacustrine notches, 155 and 148 m a.s.l., respectively, near Cueva Chica. **H:** lacustrine erosional platform carved on till, northern side of Cerro Benítez. **I:** lacustrine erosional platform carved on glaciofluvial deposits, northern side of Cerro Benítez. **J:** pavement of erratic blocks, northern side of Cerro Benítez, 135 m a.s.l. **K:** delta, northern side of the Lago Sofía valley. **L:** oblique aerial view of a 50 m high paraglacial scarp near the Mylodon Cave. **M:** 380 m high paraglacial scarp, northern side of Cerro Benítez.

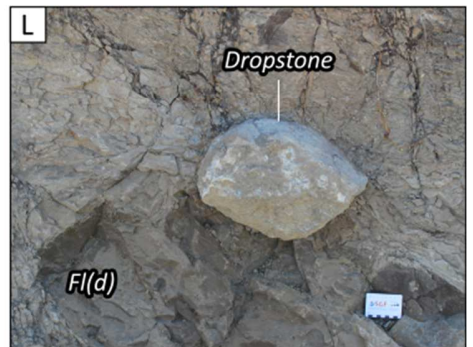
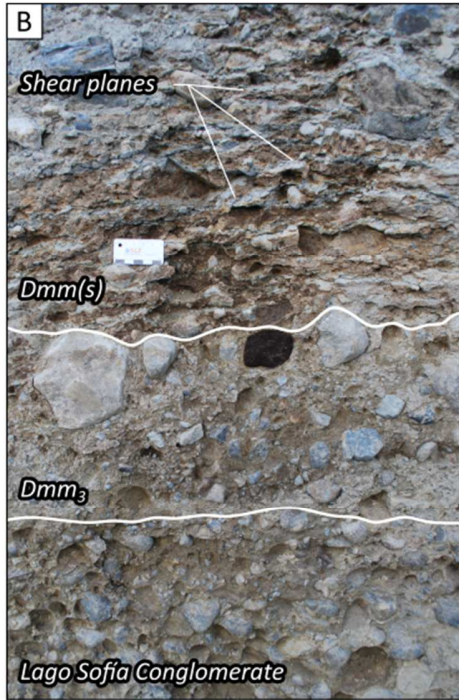
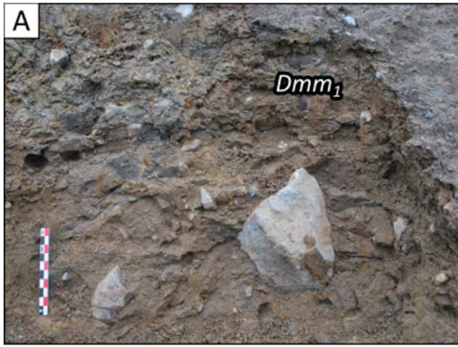


Figure 8: Sedimentary sections and facies of Cerro Benítez. **A:** till (Dmm₁), Portería section, 95 m a.s.l. **B:** subglacial till (Dmm₃, Dmm(s)), Portería section, 110 m a.s.l. **C:** subglacial till (Dmm(s)), and bevel-shaped glacial truncation of the Lago Sofía conglomerate, Silla del Diablo section, 128 m a.s.l. **D:** Los Caranchos pit, 136 m a.s.l. **E:** till, (Dmm₂), Lago Sofía section, 49 m a.s.l. **F:** till, (Dcm), Las Loicas section, 177 m a.s.l. **G:** glaciofluvial deposits (Gm), northern side of Cerro Benítez, 129 m a.s.l. **H:** Margoni pit, 128 m a.s.l. **I:** deltaic forestes (Sfo) downlapping a Gm unit, Margoni pit. **J:** ice-marginal deltaic foresets (Gfo), Los Hongos section, 115 m a.s.l. **K:** ice-marginal deltaic foresets (Gfo) truncated by a block pavement interpreted as a result of lakeshore erosion, Los Hongos section. **L:** glaustrine deposits (Fl(d)), Los Condores section, 95 m a.s.l.

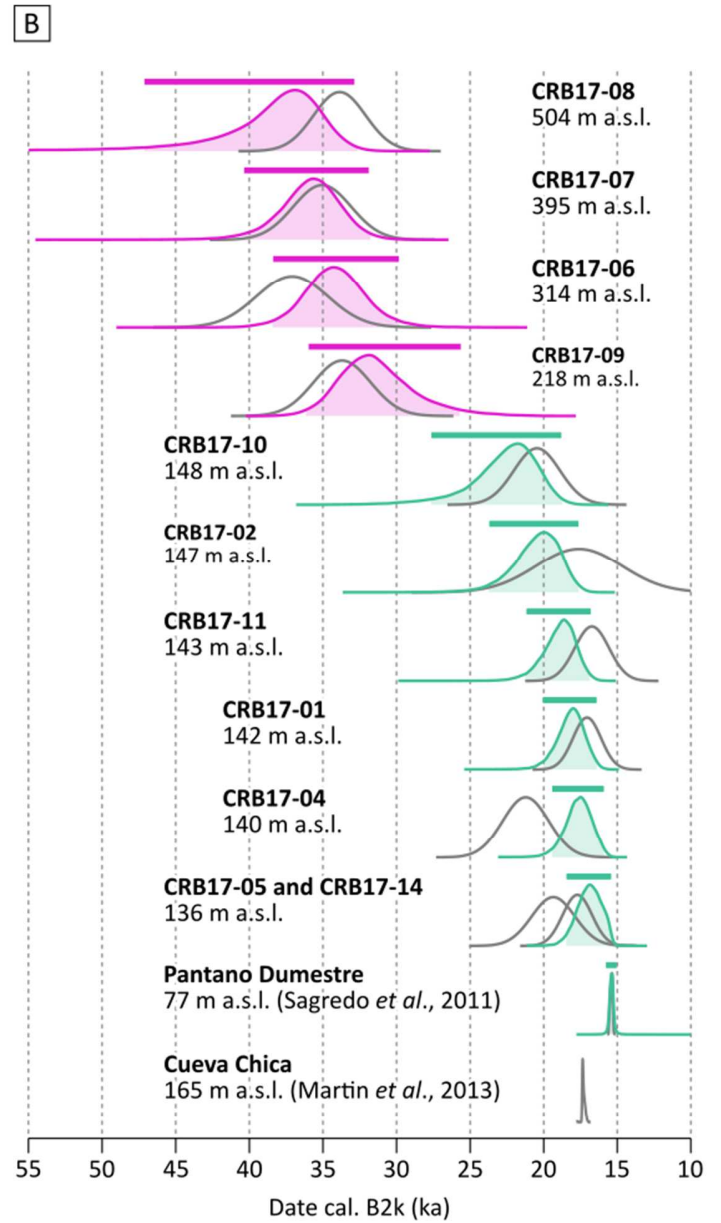
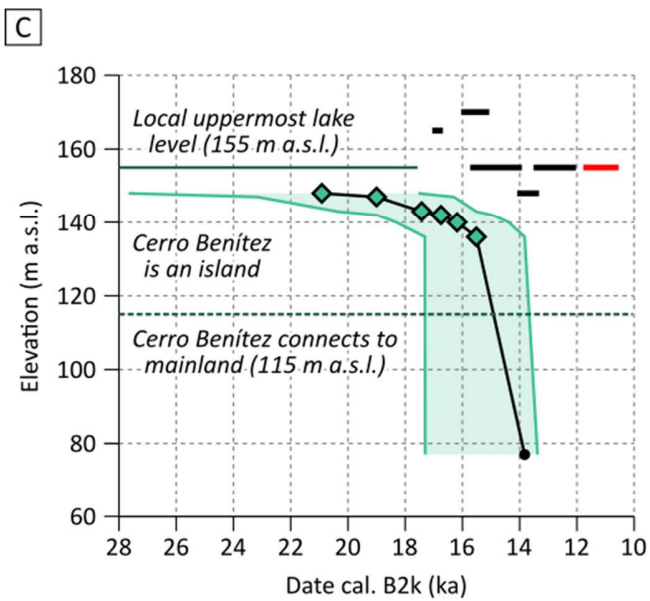
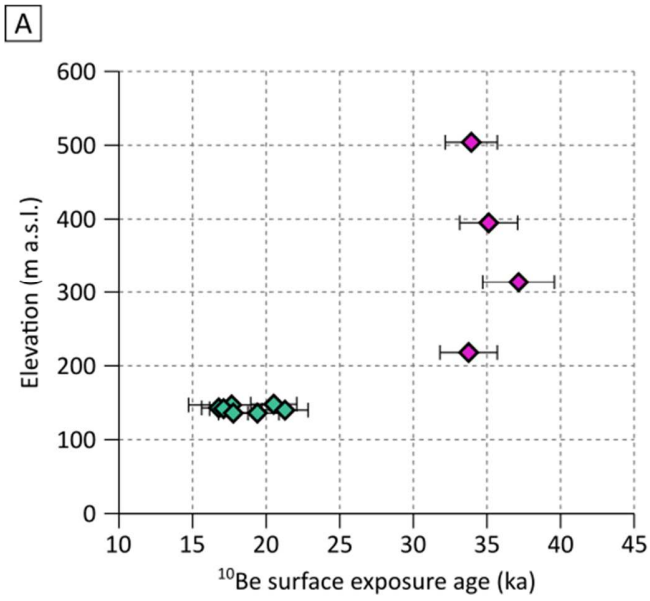


Figure 9: Prior ^{10}Be surface exposure ages of the erratic blocks and chronological model of deglaciation and lake regression. **A:** vertical distribution of the prior ^{10}Be exposure ages of the erratic blocks. **B:** probability density function of prior and posterior dates. The earliest ^{14}C age of megafaunal material from Cerro Benitez (Martin *et al.*, 2013) is featured for purpose of comparison, despite it is not included in the relative chronological model. **C:** modeled variations of the lake level through the deglaciation and chronology of the Late Pleistocene megafaunal and human occupation. HDPI: High Density Probability Interval. MAP: Maximum A posteriori Probability.

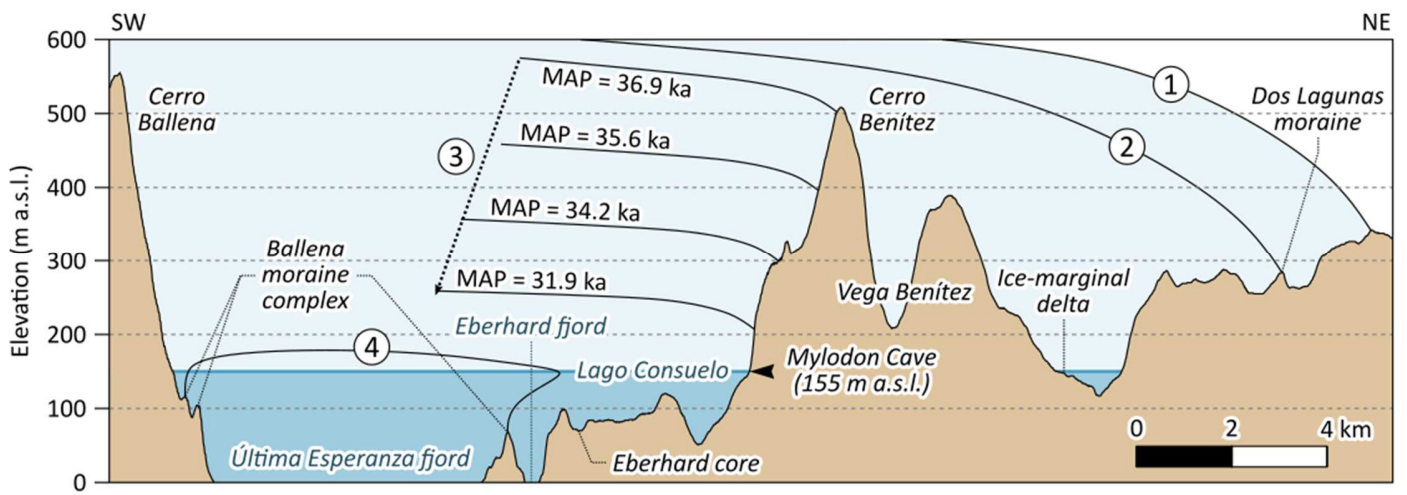


Figure 10: Elevation profile of the Última Esperanza fjord and Cerro Benítez and reconstruction of the ice sheet thickness and outermost position through the Last Glaciation. **1:** Río Turbio advance, 45.7 ka (García *et al.*, 2018). The Última Esperanza ice lobe reaches its maximal extent. **2:** Arauco advance, 34.7 ± 1.9 - 37.8 ± 4.2 ka (Sagredo *et al.*, 2011). The Última Esperanza ice lobe covers Cerro Benítez and deposits the Dos Lagunas moraine, 300 m a.s.l., 5 km to the east. **3:** Ice retreat. The Última Esperanza ice lobe divides, leaving Cerro Benítez as a nunatak. An ice-marginal delta deposits in Lago Consuelo at the eastern extremity of Cerro Benítez, 155 m a.s.l. **4:** Ballena advance. The northern tributary of the Última Esperanza ice lobe experiences a restricted readvance, and deposits the Ballena moraine complex, 5 km west of Cerro Benítez. The demise of the Última Esperanza ice lobe leaves Cerro Benítez as an island. The deglaciation of the Prat valley causes the drainage of Lago Tehuelche to Lago Consuelo. **5:** Ice retreat. **6:** present. Lago Consuelo and the Magallan lake eventually drained to the Pacific ocean.

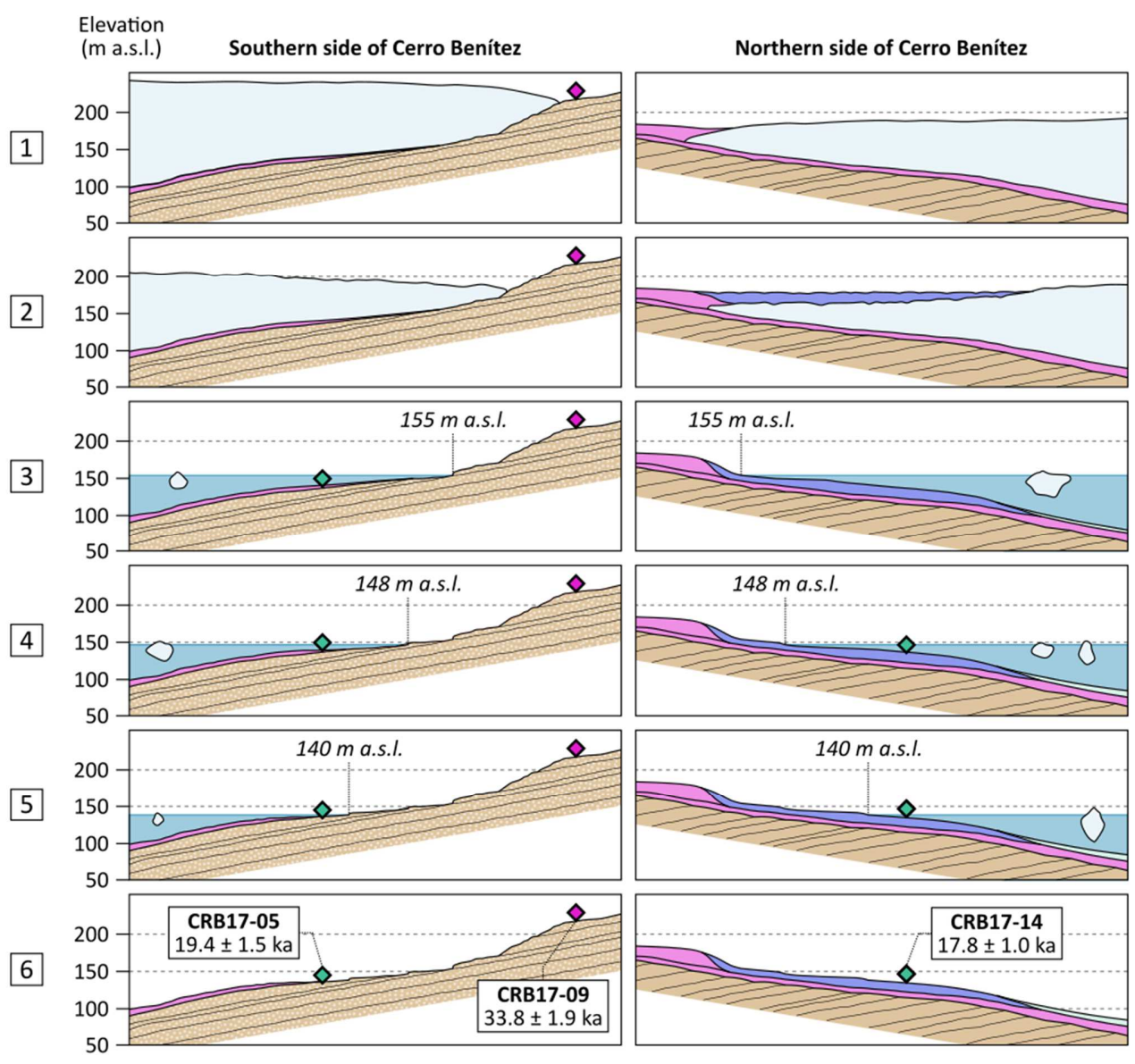


Figure 11: Hypothetical cross sections of the southern and northern sides of Cerro Benítez through the deglaciation. **1-2:** ice downwasting in the aftermath of the Arauco advance. Till and glaciofluvial deposits accumulate at the ice margin. **3-5:** definitive retreat of the ice margin and expansion of Lago Consuelo. A lacustrine erosional platform develops on bedrock and superficial deposits. Three regressive palaeoshorelines form 155, 148 and 140 m a.s.l. as the lake level gradually falls. Glaciolacustrine deposits accumulate at the bottom of the lake. **6:** drainage of Lago Consuelo.

Legend

-  Unfrozen bedrock
-  Frozen bedrock
-  Talik lower limit
-  Active layer lower limit
-  Lago Consuelo
-  Lake ice
-  Seasonal lake ice growth
-  Water migration
-  Eroded bedrock

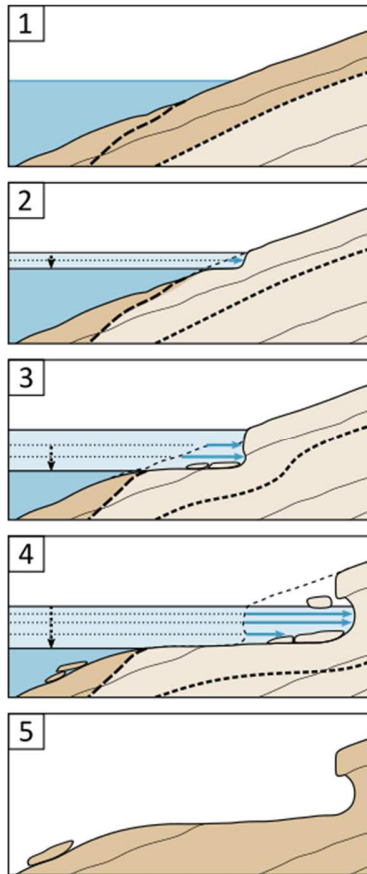


Figure 12: Model of periglacial lacustrine erosional platform development in Cerro Benítez, adapted from *Matthews et al. (1986)*. **1:** Summer. The lake surface and the active layer of the permafrost are unfrozen. **2:** Early winter. Seasonal freezing of the lake surface and active layer causes the migration of lake water toward the frozen ground. The growth of segregation ice at the interface between frozen and unfrozen ground promotes frost-shattering, initiating the development of a notch. **3:** Late winter. The notch expands downwards as the lake ice thickens. **4:** Repeated seasonal freezing cycles and clearing of the debris by the lake ice drift cause the development of a planation surface. An overhanging visor may form if the notch intercepts a stratification plane. **5:** Inherited platform after the fall of the lake level and the melt of the permafrost.

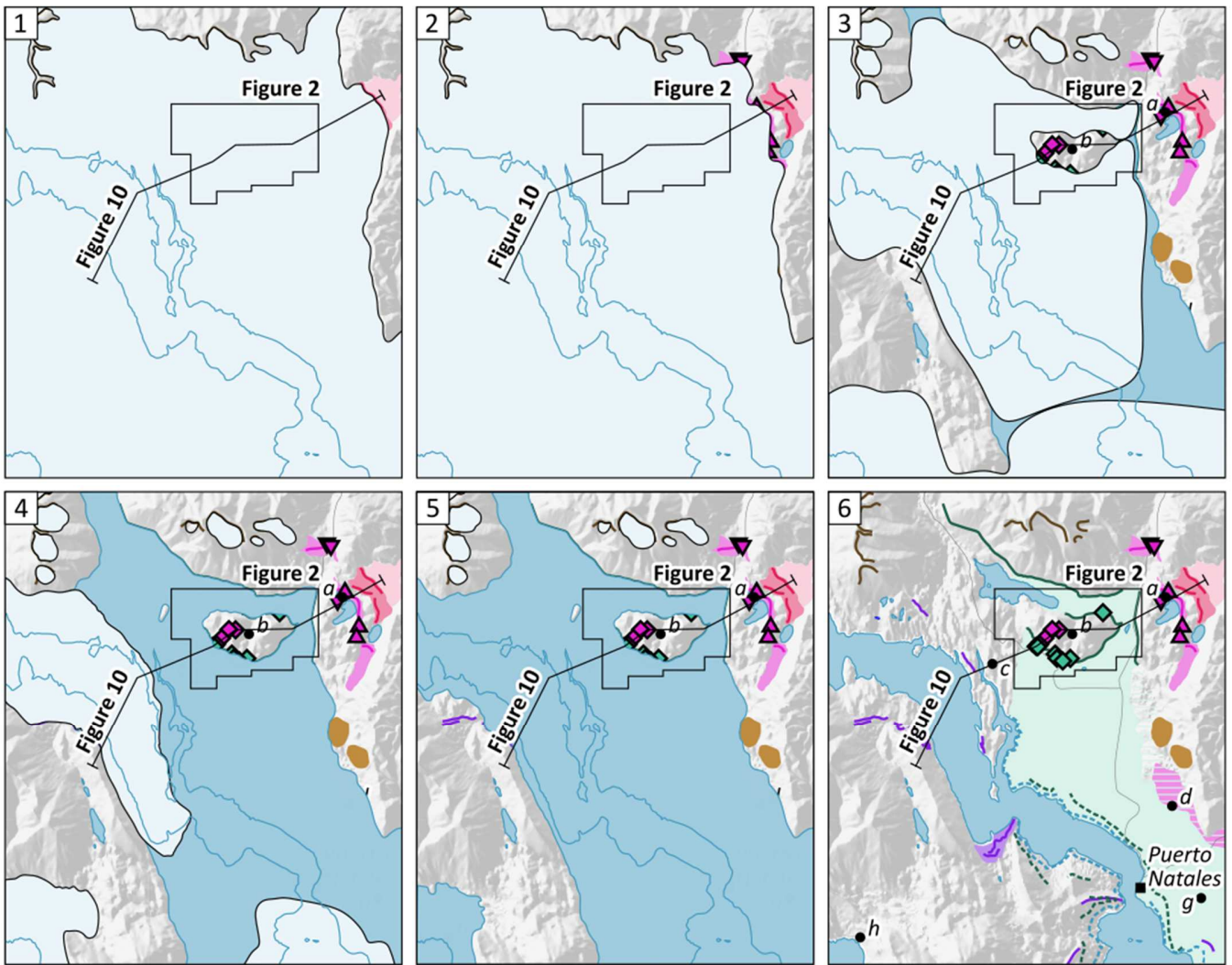


Figure 13: Reconstruction of the fluctuations of the grounded ice and ice-dammed lake extent in the area of the Última Esperanza fjord through the Last Glaciation. The position of the grounded ice margin is hypothetical in the areas lacking of moraine ridges. **1:** Río Turbio advance, 45.7 ka (García *et al.*, 2018). The Última Esperanza ice lobe reaches its maximal extent. **2:** Arauco advance, 34.7 ± 1.9 - 37.8 ± 4.2 ka (Sagredo *et al.*, 2011). The Última Esperanza ice lobe covers Cerro Benítez and deposits the Dos Lagunas moraine, 300 m a.s.l., 5 km to the east. **3:** Ice retreat. The Última Esperanza ice lobe divides, leaving Cerro Benítez as a nunatak. An ice-marginal delta deposits in Lago Consuelo at the eastern extremity of Cerro Benítez, 155 m a.s.l. **4:** Ballena advance. The northern tributary of the Última Esperanza ice lobe experiences a restricted readvance, and deposits the Ballena moraine complex, 5 km west of Cerro Benítez. The demise of the Última Esperanza ice lobe leaves Cerro Benítez as an island. The deglaciation of the Prat valley causes the drainage of Lago Tehuelche to Lago Consuelo. **5:** Ice retreat. **6:** present. Lago Consuelo and the Magallanes lake eventually drained to the Pacific ocean.

Table 1: Existing ^{14}C chronology of the Última Esperanza ice lobe retreat and regression of Lago Consuelo, based on the sedimentary and palaeontological records. ^{14}C ages were calibrated with the online ^{14}C age calculator Oxcal v4.4 using on the SHCal20 calibration curve (Hogg *et al.*, 2020). Although Alero Ovejas Muertas yielded Pleistocene megafaunal material, it has not been dated with ^{14}C yet (Martin *et al.*, submitted).

Location	Minimal date of ice margin retreat		Evidence of ice margin retreat	Elevation (m a.s.l.)	Reference
	^{14}C age	Cal. BP 2 σ probability interval			
Pantano Laurita core	9,570 \pm 40	10,684-11,096	Earliest dated lacustrine sediments	241	Sagredo <i>et al.</i> (2011)
Lago Arauco core	13,330 \pm 70	15,750-16,219	Earliest dated lacustrine sediments	180	Sagredo <i>et al.</i> (2011)
Lago Pintito core	13,670 \pm 50	16,286-16,661	Earliest dated lacustrine sediments	172	Sagredo <i>et al.</i> (2011)
Eberhard core	13,745 \pm 50	16,369-16,837	Earliest dated lacustrine sediments	68	Sagredo <i>et al.</i> (2011)
Lago Dorotea core	14,170 \pm 45	17,056-17,356	Earliest dated lacustrine sediments	260	Sagredo <i>et al.</i> (2011)
Vega Benítez core	14,520 \pm 140	17,327-18,157	Earliest dated lacustrine sediments	215	Sagredo <i>et al.</i> (2011)
Location	Minimal date of lake regression		Evidence of lake regression	Elevation (m a.s.l.)	Reference
	^{14}C age	Cal. BP 2 σ probability interval			
Pantano Antonio Varas section	9,210 \pm 40	10,239-10,492	Earliest dated peat	25	Sagredo <i>et al.</i> (2011)
Eberhard core	10,695 \pm 40	12,518-12,735	Earliest dated peat	68	Sagredo <i>et al.</i> (2011)

Cueva Lago Sofía 1	12,250 ± 110	13,802-14,830	Earliest dated megafaunal material	155	Steele and Politis (2009)
Alero Norte	12,570 ± 50	14,442-15,123	Earliest dated megafaunal material	155	Todisco <i>et al.</i> (2018)
Dos Herraduras	12,825 ± 110	14,954-15,629	Earliest dated megafaunal material	148	Martinic (1996)
Alero Los Bloques	12,870 ± 50	15,152-15,548	Earliest dated megafaunal material	148	Todisco <i>et al.</i> (2018)
Pantano Dumestre core	12,910 ± 25	15,249-15,555	Earliest dated peat	77	Sagredo <i>et al.</i> (2011)
Cueva de la Ventana	13,270 ± 140	15,489-16,332	Earliest dated megafaunal material	155	Todisco <i>et al.</i> (2018)
Cueva Lago Sofía 4	13,545 ± 100	15,974-16,621	Earliest dated megafaunal material	155	Labarca and Prieto (2009)
Cueva del Medio	13,790 ± 60	16,429-16,941	Earliest dated megafaunal material	155	Martin <i>et al.</i> (2015)
Cueva Ciro	13,840 ± 150	16,254-17,230	Earliest dated megafaunal material	155	Todisco <i>et al.</i> (2018)
Cueva Escondida	13,890 ± 60	16,599-17,028	Earliest dated megafaunal material	155	Martin and Borrero (2017)
Myloodon Cave	13,980 ± 50	16,717-17,092	Earliest dated megafaunal material	155	Todisco <i>et al.</i> (2018)
Cueva Nordenskjöld	13,990 ± 150	16,501-17,370	Earliest dated megafaunal material	170	Martin and Borrero (2017)

Cueva Chica	14,870 ± 70	17,942-18,270	Earliest dated megafaunal material	165	Martin <i>et al.</i> (2013)
Location	Minimal date of human occupation		Evidence of human occupation	Elevation (m a.s.l.)	Reference
	¹⁴ C age	Cal. BP 2σ probability interval			
Cueva del Medio	11,120 ± 130	13,233-12,754	Earliest dated megafaunal material within archaeological unit	155	Nami and Nakamura, 1995
Cueva del Medio	11,040 ± 250	13,461-12,481			
Cueva Lago Sofía 1	11,570 ± 60	13,576-13,301	Earliest dated hearth charcoal	155	Prieto, 1991

Table 2: Compilation of ^{10}Be surface exposure ages of erratic blocks from the area of the Última Esperanza ice lobe, at the exception of those identified by the authors as outliers. ^{10}Be ages surface exposure ages obtained by Sagredo *et al.* (2011) and García *et al.* (2018) were recalculated with different production rates and scaling schemes. We used the online exposure age calculator CRONUS v3 (<https://hess.ess.washington.edu>; Balco *et al.*, 2008). Erosion was neglected and snow correction was not applied, in agreement with Sagredo *et al.* (2011) and García *et al.* (2018). *: production rate and scaling scheme used in the discussion.

Sample	Kaplan <i>et al.</i> (2011) production rate						Borchers <i>et al.</i> (2016) production rate*							Landform	Referenc e
	St scaling scheme		Lm scaling scheme		LSDn scaling scheme		St scaling scheme		Lm scaling scheme		LSDn scaling scheme*				
	10Be age (ka)	External error (ka)	10Be age (ka)	External error (ka)	10Be age (ka)	External error (ka)	10Be age (ka)	External error (ka)	10Be age (ka)	External error (ka)	10Be age (ka)	External error (ka)	Median age (ka)		
TUR-13-02	53.5	4.9	52.3	4.8	50.9	4.6	49.7	3.3	49.0	3.0	49.5	3.0	45.7	Río Turbio moraine complex	García <i>et al.</i> (2018)
TUR-13-14	51.1	4.9	49.9	4.8	48.6	4.6	47.5	3.4	46.8	3.2	47.2	3.2			
TUR-13-13	49.7	4.6	48.6	4.5	47.2	4.3	46.3	3.1	45.6	2.8	45.9	2.9			
TUR-13-11	49.5	5.1	48.3	5.0	47.0	4.8	46.0	3.7	45.3	3.5	45.7	3.5			
TUR-13-12	49.5	4.9	48.3	4.8	47.0	4.6	46.0	3.5	45.3	3.3	45.7	3.3			
TUR-13-16	47.8	4.4	46.7	4.3	45.4	4.2	44.5	3.0	43.8	2.7	44.2	2.8			
TUR-13-08	47.8	4.5	46.7	4.4	45.4	4.3	44.5	3.1	43.8	2.9	44.1	2.9			
TUR-13-15	47.5	4.6	46.4	4.5	45.1	4.4	44.2	3.3	43.5	3.1	43.9	3.1			
PN-04-08	40.6	5.3	39.7	5.2	38.8	5.1	37.8	4.3	37.3	4.2	37.8	4.2	36.0	Dos Lagunas	Sagredo <i>et al.</i>
HUG-05-03	38.7	3.5	37.9	3.4	37.0	3.3	36.1	2.3	35.6	2.1	36.0	2.2			

HUG-05-02	37.3	3.2	36.5	3.2	35.6	3.1	34.7	2.1	34.2	1.9	34.7	1.9		moraine	(2011)
DOR-12-08	37.1	4.1	36.3	4.0	35.5	3.9	34.5	3.1	34.1	2.9	34.5	3.0	32.4	Arauco moraine complex and Dos Lagunas moraine	García <i>et al.</i> (2018)
DOR-12-09	35.9	4.0	35.1	3.9	34.3	3.8	33.4	3.1	33.0	2.9	33.4	3.0			
DOR-12-02	35.7	3.3	34.9	3.2	34.2	3.1	33.2	2.2	32.8	2.1	33.2	2.1			
AR-13-08	35.1	3.2	34.3	3.2	33.5	3.1	32.6	2.2	32.2	2.0	32.6	2.0			
AR-13-07	34.9	3.2	34.2	3.1	33.4	3.1	32.5	2.2	32.1	2.0	32.5	2.0			
AR-13-09	34.9	4.2	34.2	4.1	33.3	4.0	32.5	3.3	32.1	3.1	32.4	3.2			
AR-13-23	34.8	4.5	34.1	4.4	33.2	4.3	32.4	3.7	32.0	3.5	32.3	3.6			
AR-13-22	34.3	3.2	33.5	3.1	32.7	3.0	31.9	2.2	31.5	2.0	31.8	2.1			
AR-12-06	34.0	4.1	33.3	4.0	32.4	3.9	31.6	3.3	31.2	3.1	31.5	3.2			
AR-12-07	33.6	4.6	32.9	4.5	32.1	4.3	31.3	3.8	30.9	3.6	31.2	3.7			
AR-13-17	32.1	3.0	31.4	2.9	30.6	2.8	29.9	2.1	29.5	1.9	29.8	1.9			
AR-13-18	31.3	3.0	30.6	3.0	29.9	2.9	29.1	2.2	28.8	2.0	29.1	2.0			
CRB17-06	40.0	3.8	39.1	3.7	38.2	3.6	37.2	2.6	36.7	2.4	37.1	2.4		Cerro Benítez	This study
CRB17-07	37.8	3.3	36.9	3.2	36.1	3.1	35.2	2.1	34.7	1.9	35.1	2.0			
CRB17-08	36.5	3.1	35.7	3.0	34.9	3.0	34.0	1.9	33.5	1.7	33.9	1.8			
CRB17-09	36.3	3.2	35.5	3.2	34.7	3.1	33.8	2.1	33.4	1.9	33.8	1.9			

CRB17-04	22.7	2.3	22.3	2.2	21.8	2.2	21.1	1.6	21.0	1.5	21.3	1.6	Lacustrine erosional platform	This study
CRB17-10	21.9	2.2	21.5	2.2	21.1	2.1	20.3	1.6	20.2	1.5	20.5	1.6		
CRB17-05	20.6	2.1	20.3	2.1	19.9	2.0	19.2	1.5	19.1	1.4	19.4	1.5		
CRB17-14	18.8	1.7	18.6	1.6	18.2	1.6	17.5	1.1	17.5	1.0	17.8	1.0		
CRB17-02	18.7	3.3	18.5	3.3	18.1	3.2	17.4	2.9	17.3	2.9	17.7	2.9		
CRB17-01	18.1	1.6	17.9	1.6	17.6	1.5	16.9	1.0	16.8	0.9	17.1	1.0		
CRB17-11	17.8	1.7	17.5	1.7	17.2	1.7	16.5	1.2	16.5	1.1	16.8	1.2		

Table 3: Identification criteria and palaeoenvironmental significance of landforms and deposits mapped from the remote-sensing data interpretation at the scales of 1/500,000 and 1/50,000, adapted from Glasser and Janson (2008), Darvill *et al.* (2014) and Bendle *et al.* (2017).

Landforms and deposits	Identification criteria	Risk of confusion	Environment	Previous mapping	Scale of mapping	
					1 :500,000	1 :50,000
Glacial cirque	Semicircular depression, often overdeepened, delimited by steep ridges carved on the mountain slope	Large mass-wasting scars can be mistaken for glacial cirque, but they are steeper, not overdeepened and more isolated	Subglacial	Glasser and Janson (2008)	x	
Drumlin	Parallel, rectilinear hills with a steep up-flow side and a gentle down-flow side	Deflation surfaces on the western shore of Lago Balmaceda were misidentified as glacial lineations by Glasser and Janson (2008) and Darvill <i>et al.</i> (2014)	Subglacial	Glasser and Janson (2008), Darvill <i>et al.</i> (2014), García <i>et al.</i> (2018)	x	
Moraine ridge	Concentric, curvilinear, often discontinuous ridges, gently dipping down-stream	Palaeoshorelines were misidentified as moraine ridges on the northern side of Lago Sofia by Glasser and Janson (2008)	Ice-marginal (glacial)	Caldenius (1932), Glasser and Janson (2008), Sagredo <i>et al.</i> (2011), Darvill <i>et al.</i> (2014), García <i>et al.</i> (2014), García <i>et al.</i> (2018)	x	x
Kame terrace	Gently sloping, depositional surface raised above the	A lacustrine erosional platform was	Ice-marginal (glaciofluvial)	None	x	

	valley floor, buttressed on the mountain slope or a moraine ridge	misidentified as a kame terrace by García <i>et al.</i> (2018)				
Outwash plain	Flat depositional surface backed upstream by frontal moraine ridges	None	Proglacial (glaciofluvial)	Glasser and Janson (2008), Darvill <i>et al.</i> (2014), García <i>et al.</i> (2014), García <i>et al.</i> (2018)	x	
Palaeoshoreline	Linear, subhorizontal concave break in the slope caused by lake or seashore erosion, restricted to a closed or formerly ice-dammed depression	Homoclinal scarps can be mistaken for palaeoshorelines, but they are not horizontal in all directions	Proglacial (glaciolacustrine)	Glasser and Janson (2008), Darvill <i>et al.</i> (2014), García <i>et al.</i> (2018)	x	x
Erosional platform	Erosional surface carved on ice-marginal deposits or bedrock, delimited to the top by a palaeoshoreline and gently sloping to the palaeolake side	Kame terraces can be mistaken for erosional platforms carved on ice-marginal deposits, but erosional platforms are also traceable on the outcropping bedrock	Proglacial (glaciolacustrine)	Sagredo <i>et al.</i> (2011)	x	x
Delta	Fan-shaped depositional surface at the outlet of a valley, gently dipping to the palaeolake side and flanked by palaeoshorelines	None	Proglacial (glaciolacustrine)	None	x	x

Lakeshore deposits	Elongate depositional surfaces parallel to the palaeoshorelines, gently dipping to the palaeolake side and occurring as raised beaches, barriers and spits	None	Proglacial (glaciolacustrine)	None	x	x
Glaciolacustrine deposits	Smooth depositional surface restricted to the palaeolake basin and vertically extending up to the palaeoshoreline	None	Proglacial (glaciolacustrine)	García <i>et al.</i> (2018)	x	x
Paraglacial rockslope failure deposits	Mound at the foot of a semicircular scar of similar diameter, carved on a former ice-contact slope	None	Paraglacial	None	x	x
Alluvial fan	Fan-shaped depositional surface at the foot of the slope	Deltas may be mistaken for alluvial fans, but they are flatter as the elevation of the deposits is primarily controlled by the palaeolake level	Fluvial	García <i>et al.</i> (2018)	x	x
Alluvial terrace	Flat depositional surface restricted to a fluvial valley, dissected by a river and gently sloping downstream	None	Fluvial	García <i>et al.</i> (2018)	x	
Gorge	Linear depression incised by a river and delimited by	None	Fluvial	None		x

	steep slopes, attesting to base level lowering					
Gully	Linear depression caused by intermittent surface runoff erosion on a slope	None	Fluvial	None		x

Table 4: Macroscopic sedimentary facies of the superficial deposits of Cerro Benítez. The terminology used in facies description is taken from Evans and Benn (2004). Palaeoenvironmental interpretation is based on Brodzikowski and van Loon (1987) and Evans, (2003).

Code	Facies	Gravel surface aspect	Depositional structures	Deformation structures	Depositional process	Depositional environment	Superficial deposits
Dmm(s)	Sheared, unsorted matrix-supported diamicton (20 to 40 % of clasts)	Sharp-edged angular	Massive	Anastomosed , subhorizontal fractures	Subglacial lodgement of ice-tracted reworked debris	Subglacial	Subglacial till; “lodgement till” sensu Brodzikowski and van Loon (1987); “subglacial traction till” sensu Evans <i>et al.</i> (2006)
Dmm1	Unsorted matrix-supported diamicton (2 to 5 % of clasts)	Sharp-edged angular	Massive	None	-	-	Till
Dmm2	Unsorted matrix-supported diamicton (20 % of clasts)	Sharp-edged angular	Massive	None	-	-	Till
Dmm3	Unsorted matrix-supported diamicton (40 % of clasts)	Sharp-edged angular	Massive	None	-	-	Till
Dcm	Sandy matrix clast-supported diamicton	Sharp-edged angular to moderately rounded	Massive	None	-	-	Till
Gm	Sandy matrix clast-supported gravels	Smooth-edged angular to well-rounded	Massive	None	High-energy channel lag	Glaciofluvial	Glaciofluvial deposits
Gfo	Gravel foresets	Smooth-edged angular to well-	Foreset bedding, subordinate backset	None	High-energy deltaic progradation	Glaciofluvial	Ice-marginal deltaic foresets

		rounded	bedding				
Sfo	Sand foresets	No gravel	Foreset bedding, subordinate cross bedding	None	Moderate-energy deltaic progradation	Glaciofluvial or fluvial	Ice-marginal deltaic or deltaic foresets
Fl(d)	Laminated silts and clays with dropstones	No gravel	Laminae	Laminae compacted by dropstone	Decantation of periodic turbid plume (silts and clays), ice-rafted debris fall (dropstones)	Glaciolacustrine	Glaciolacustrine deposits

Table 5: Be isotope ratios and ^{10}Be surface exposure ages of erratic blocks from Cerro Benítez. Measured $^{10}\text{Be}/^9\text{Be}$ ratios were normalized to the 07KNSTD standard and corrected with a mean procedural blank $^{10}\text{Be}/^9\text{Be}$ ratio of 3.75×10^{-15} . Surface exposure ages were calculated with the online surface exposure age calculator CRONUS v3 10Be (<https://hess.ess.washington.edu>; Balco et al., 2008) using the production rate model of Borchers *et al.* (2016) and the Lifton-Sato flux scaling scheme (Lifton *et al.*, 2014). Sample density was assumed as 2.65 g.cm^{-3} . Sample thickness and topographic shielding corrections were applied. Erosion was neglected, because unequivocally weathered surfaces were not sampled. Snow correction was not applied, in agreement with Sagredo *et al.* (2011) and García *et al.* (2018).

Sample	Latitude (WGS 1984)	Longitude (WGS 1984)	Elevation (m a.s.l.)	Thickness (cm)	Topographic shielding factor	Dissolved quartz mass (g)	^9Be mass in carrier (μg)	$^{10}\text{Be}/^9\text{Be}$ ($\times 10^{-15}$)	Error ($\times 10^{-15}$)	^{10}Be concentration (atom.g^{-1})	Error (atom.g^{-1})	^{10}Be age (ka)	Internal error (ka)	External error (ka)
CRB17-06	-51.5604	-72.6133	314	1.5	0.99950	3.229	221.33430	52.288	1.954	224632.5	9972.8	37.1	1.7	2.4
CRB17-07	-51.5546	-72.6054	395	1.5	0.99764	5.923	221.07960	94.835	2.229	228431.0	6665.7	35.1	1.0	2.0
CRB17-08	-51.5548	-72.5983	504	1.5	0.99973	17.946	221.67390	299.190	4.435	244278.5	5083.3	33.9	0.7	1.8
CRB17-09	-51.5645	-72.6189	218	1.5	0.99916	14.886	215.33400	198.690	5.693	186386.4	5974.6	33.8	1.1	1.9
CRB17-04	-51.5660	-72.6210	140	1	0.99671	5.066	225.67345	39.105	1.902	108727.6	6097.9	21.3	1.2	1.6
CRB17-10	-51.5738	-72.5861	148	2	0.98287	4.119	225.84435	30.751	1.514	103225.8	6120.5	20.5	1.2	1.6
CRB17-05	-51.5658	-72.6227	136	1	0.99745	4.993	221.67390	36.456	1.771	98539.9	5765.7	19.4	1.1	1.5

CRB17-14	-51.5434	-72.5511	136	3	0.99860	17.264	221.92860	106.430	2.625	88642.7	2651.5	17.8	0.5	1.0
CRB17-02	-51.5709	-72.6023	147	1	0.98645	0.973	220.74000	9.152	0.688	89403.6	14126.4	17.7	2.8	2.9
CRB17-01	-51.5737	-72.6004	142	1	0.99763	15.574	220.74000	95.239	2.212	87119.8	2520.7	17.1	0.5	1.0
CRB17-11	-51.5755	-72.5942	143	1.5	0.99949	11.527	221.67390	69.618	3.131	85298.0	4290.3	16.8	0.8	1.2

Table 6: Prior ages and posterior age distributions obtained with the chronological modelling software ChronoModel v2.0.18 (<https://github.com/Chronomodel/chronomodel>; Lanos and Philippe, 2015; Lanos and Dufresne, 2019). MAP: Maximum A posteriori Probability; HDPI: High Probability Density Interval.

Sample	Prior age (ka)	Event	MAP (ka B2k)	Mean (ka B2k)	σ (ka B2k)	HPDI 95% (ka B2k)
CRB17-08	33.9 ± 1.8	Ice downwasting < 504 m a.s.l.	36.9	38.6	3.9	32.6-47.1
CRB17-07	35.1 ± 2.4	Ice downwasting < 395 m a.s.l.	35.6	35.9	2.2	31.7-40.3
CRB17-06	37.1 ± 2.4	Ice downwasting < 314 m a.s.l.	34.2	34.1	2.2	29.8-38.4
CRB17-09	33.8 ± 1.9	Ice downwasting < 218 m a.s.l.	31.9	31.3	2.6	25.7-36.1
CRB17-10	20.5 ± 1.6	Lake regression < 148 m a.s.l.	21.7	22.7	2.3	18.7-27.7
CRB17-02	17.7 ± 2.9	Lake regression < 147 m a.s.l.	20.0	20.5	1.6	17.6-23.7
CRB17-11	16.8 ± 1.2	Lake regression < 143 m a.s.l.	18.6	19.0	1.1	16.9-21.2
CRB17-01	17.1 ± 1.0	Lake regression < 142 m a.s.l.	18.0	18.2	0.9	16.4-20.0
CRB17-04	21.3 ± 1.6	Lake regression < 140 m a.s.l.	17.5	17.6	0.9	15.9-19.4
CRB17-05	19.4 ± 1.5	Lake regression < 136 m a.s.l.	16.9	16.9	0.8	15.4-18.5
CRB17-14	17.8 ± 1.0					
Pantano Dumestre core (Sagredo <i>et al.</i> , 2011)	15.2-15.6 cal. BP	Lake regression < 77 m a.s.l.	15.4	15.4	0.2	15.0-15.7

Table 7: Synthetic chronology of the Última Esperanza ice lobe advances and retreats and the regression of Lago Consuelo in Cerro Benítez, during the Last Glaciation. Dates from this study refer to the MAP obtained from chronological modelling (Table 6).

Date	Event	Local ice-dammed lake level	Erosional landforms	Superficial deposits	Accessibility of Cerro Benítez to the megafauna
45.7 ka (García <i>et al.</i> , 2018)	Río Turbio advance	-	-	-	Subglacial bed
34.7 ± 1.9-37.8 ± 4.2 ka (Sagredo <i>et al.</i> , 2011)	Arauco advance	-	-	-	
36.9 to 31.9 ka cal. B2k (this study)	Ice downwasting	155 m a.s.l.	Roches moutonnées Subglacial meltwater channels	Till Glaciofluvial deposits Ice-marginal delta	Nunatak
Between 31.9 and 16.9 ka cal. B2k (this study)	Glacial readvance in the Última Esperanza fjord	155 m a.s.l.			
21.7 to 16.9 cal. B2k (this study)	Slow lake regression controlled by post-glacial isostatic rebound	155 to 136 m a.s.l.	Lacustrine erosional platform Paraglacial slopes	Delta Glaciolacustrine deposits	Island
17.9-18.3 ka cal. BP (Martin <i>et al.</i> , 2013)	Earliest evidence of megafaunal presence in Cerro Benítez	143-140 m a.s.l.			
16.9 to 15.4 ka cal. B2k (Sagredo <i>et al.</i> , 2011; this study)	Fast lake regression controlled by the drainage reversal to the Magellan lake	136 to 77 m a.s.l.	Gullies	Alluvial fans	Cerro Benítez connects to Sierra Dorotea as the ice-dammed lake level falls below 115 m a.s.l.